

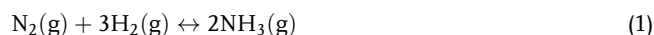
Recent Progress of the Design and Engineering of Bismuth Oxyhalides for Photocatalytic Nitrogen Fixation

Peishen Li, Shuai Gao, Qiming Liu, Peiren Ding, Yunyun Wu, Changzheng Wang,*
Shaobin Yu, Wen Liu, Qiang Wang,* and Shaowei Chen*

Photocatalytic nitrogen fixation represents an effective technology for the artificial production of ammonia from atmospheric nitrogen, a critical step toward a sustainable economy. Bismuth oxyhalides (BiOX, X = Cl, Br, and I) have emerged as viable catalysts for photocatalytic reduction of nitrogen into ammonia, due to their unique electronic structures and optical properties. Herein, the recent progress of BiOX-based photocatalysts for nitrogen fixation, with a focus on the reaction mechanism and pathways, materials preparation, and strategies of structural engineering for enhanced performance, is summarized. The article is concluded with a perspective where the promises and challenges of bismuth-based photocatalysts for nitrogen reduction to ammonia are highlighted, along with possible future research directions.

1. Introduction

Ammonia (NH₃) has been used extensively across the globe as an effective plant fertilizer in agricultural production,^[1–3] and recently also emerged as a new clean energy and fuel.^[4,5] Traditionally, ammonia is produced predominantly by the enzymatic processes in plants and microorganisms (150–200 Tg yearly).^[6,7] Yet, such a productivity cannot meet the ever increasing demand of ammonia with the rapid expansion of human population.^[7–10] In 1909, the invention of the Haber–Bosch method led to a significant leap in NH₃ production,^[2,11,12] which is depicted below



and represents a significant breakthrough in the history of artificial nitrogen fixation.^[13–15] In fact, this reaction has thus far been the subject of three chemistry Nobel prizes, one for the discovery of the reaction,^[16] a second for the development of high-pressure industrial processes,^[17] and a third for the study of the fundamental surface chemistry on the catalysts.^[18] In fact, the Haber–Bosch process has been heralded as the most important invention of the 20th century, which revolutionizes the nitrogen conversion to ammonia.^[14,19]

However, due to the high stability of N₂ (bond energy 941.3 kJ mol^{−1}),^[20,21] nitrogen fixation by the Haber–Bosch process necessitates operation with catalysts under high temperatures and high pressures.^[22,23] This consumes a substantial amount of energy, greatly increases the cost of NH₃ production,^[24,25] and causes serious environmental pollution.^[21] In practice, the reactant gases need to be heated to 400–450 °C at a pressure of 150–200 atm,^[26,27] with the addition of Fe-based catalysts.^[27,28] Meanwhile, a significant amount of energy needs to be invested to remove as much oxygen as possible from air to minimize catalyst oxidation.^[29] After the deaeration step, the dissociated mixture of nitrogen and hydrogen forms ammonia on the iron-based catalyst.^[30] Thus, this process is rather costly.^[31]


In a practical operation, the fixation of nitrogen to ammonia is completed in a high-pressure synthetic tower. The nitrogen and hydrogen gases are first mixed and compressed into the converter chamber from the top,^[32,33] pass the heat exchanger at the bottom to increase the gas temperature, and then enter the contact chamber where Fe-based catalysts drives the production of ammonia. Note that only part of the nitrogen reacts with hydrogen to produce ammonia.^[34] The mixture of nitrogen,

P. Li, S. Gao, P. Ding, Y. Wu, Prof. Q. Wang
Laboratory for Micro-sized Functional Materials
College of Elementary Education
Department of Chemistry
Capital Normal University
Beijing 100048, China
E-mail: qwchem@gmail.com

Q. Liu, Prof. S. Chen
Department of Chemistry and Biochemistry
University of California
1156 High Street, Santa Cruz, CA 95064, USA
E-mail: shaowei@ucsc.edu

Prof. C. Wang, S. Yu
Beijing Key Laboratory of Functional Materials for Building Structure and Environmental Remediation
Beijing University of Civil Engineering and Architecture
Beijing 100044, China
E-mail: changzhwang@163.com

P. Li, Prof. W. Liu
Beijing Innovation Center for Engineering Science and Advanced Technology (BIC-ESAT)
Key Laboratory of Water and Sediment Sciences (Ministry of Education)
College of Environmental Sciences and Engineering
Peking University
Beijing 100871, China

 The ORCID identification number(s) for the author(s) of this article can be found under <https://doi.org/10.1002/aesr.202000097>.

© 2021 The Authors. Advanced Energy and Sustainability Research published by Wiley-VCH GmbH. This is an open access article under the terms of the Creative Commons Attribution License, which permits use, distribution and reproduction in any medium, provided the original work is properly cited.

DOI: 10.1002/aesr.202000097

hydrogen, and ammonia then leaves the converter through a heat exchanger,^[35] where ammonia will be liquefied through a condenser, and separated from the mixture.^[36] The remaining nitrogen and hydrogen is again compressed and fed into the synthetic tower to start a second cycle. In this operation, raw materials are saved and recycled to maximize the fixation efficiency.^[35] Yet, many issues remain, in particular, low conversion rate of nitrogen to ammonia, high energy consumption, and serious pollution.^[37] In fact, the Haber–Bosch process accounts for nearly 2% of global energy consumption, and is responsible for ≈1% of the global greenhouse gas emissions. Therefore, the development of new, effective nitrogen fixation technologies is highly desired that are lower-cost, high-performance, and environment-friendly.^[7,10,12,38]

In 1967, Fujishima and Honda accidentally discovered that under ultraviolet irradiation, titanium dioxide (TiO₂) single crystal can split water into oxygen and hydrogen.^[39] Such a photocatalytic technology has since been exploited for a wide range of applications. For instance, in 1977, Schrauzer et al. demonstrated, for the first time ever, that TiO₂ can also be used as a photocatalyst for nitrogen fixation,^[40] and in 1980, Schrauzer and Guth reported the first rigorous study of photocatalytic nitrogen fixation by natural materials.^[41] These are just among the numerous studies on photocatalytic nitrogen fixation, a field that is booming rapidly.^[42,43]

In photocatalysis, design and engineering of effective semiconductor catalysts is a critical first step. Among these, bismuth-based materials have been attracting extensive attention, due to their low bandgap energy and high electrical conductivity.^[44] Harriman et al.^[45] were the first to report the photocatalytic activity of Bi₂O₃. In recent years, bismuth oxyhalides (BiOX, X = Cl, Br, and I) have emerged as a unique class of photocatalysts due to their high photocatalytic activity and stability. For instance, Li et al.^[46] in 2015 reported that BiOBr nanosheets exhibited efficient nitrogen fixation under visible light irradiation, where oxygen vacancies (OVs) on the exposed surface significantly enhanced the adsorption and activation of N₂. Indeed, the photocatalytic performance can be significantly improved with an increase in the OV concentration and separation rate of photogenerated electron–hole pairs.^[12,32] This important breakthrough essentially opens a door of photocatalytic nitrogen fixation based on BiOX materials.^[47,48]

Thus far, it has been well-known that adsorption of N₂ onto the catalyst surface plays a key role in determining the photocatalytic efficiency of nitrogen fixation,^[43,49] which can be facilitated by the formation of OVs.^[1,50–53] Note that OVs are the most prevalent and widely studied anion defects with a relatively low formation energy on oxide surfaces,^[13,54,55] and can act as electron traps to effectively capture and activate inert gas molecules, such as O₂, CO₂, and N₂.^[46,56] However, surface OVs introduced artificially can be easily oxidized, leading to cessation of N₂ activation in the fixation process,^[12,57] and a large surface area is needed to maximize the production of OVs.^[54] Therefore, substantial efforts have been devoted to the structural engineering of BiOX for the formation of abundant and stable OVs so as to enhance the performance of photocatalytic nitrogen fixation.^[48,58]

In this review article, we summarize recent progress in the design and engineering of BiOX-based materials for photocatalytic nitrogen fixation, within the context of sample synthesis,

structural characterization, and OV formation. The corresponding structure–activity correlation is then exploited for the establishment of the reaction mechanism and pathway. We conclude the review with a perspective where the challenges of photocatalytic nitrogen fixation are highlighted, along with possible further research directions.

2. Bismuth-Based Photocatalysts for Nitrogen Fixation

Photocatalytic nitrogen fixation started as early as in the 1940s (Figure 1). The purpose of the early work was to study the natural nitrogen fixation of soil, rather than artificial fixation by metals and metal oxides.^[19,45] For instance, Dhar et al.^[59] disinfected soil obtained from the field, and observed apparent nitrogen fixation both under photoirradiation and in the dark, with a higher rate for the former than for the latter. However, the results were not reproducible later on, likely because of the limited conditions at the time, such that the sterilization procedure used did not deactivate all nitrogen fixing bacteria. In addition, the fact that non-zero production of ammonia was observed even in the control experiment suggested that the photolysis of amino acids in dead microorganisms might be responsible for part of the ammonia produced. Although there was no clear concept of photocatalytic nitrogen fixation at that time and the conclusions obtained from the research were somewhat skeptical, it is nonetheless the first demonstration of photocatalytic nitrogen fixation. Later in 1977, Schrauzer et al.^[40] reported the first photocatalytic nitrogen fixation by Fe-doped TiO₂. Experimentally, they observed that in an argon atmosphere, the photolysis of chemisorbed water on partially outgassed TiO₂ powders produced H₂ and O₂ at a molar ratio of 2:1; yet, in the presence of molecular nitrogen, O₂ can still be formed, but the formation of H₂ was inhibited because chemically adsorbed nitrogen was reduced to NH₃ and trace N₂H₄, $N_2 + 3H_2O + nh\nu \rightarrow 2NH_3 + 1.5O_2$ and $N_2 + 2H_2O + mh\nu \rightarrow N_2H_4 + O_2$. The doping of iron improved the photocatalytic activity of rutile TiO₂, which was used in a prototype solar cell for the photochemical synthesis of ammonia with N₂ and H₂O.

Since then, semiconductor photocatalysts have been used extensively in photocatalytic nitrogen fixation. Among these, bismuth-based materials have emerged as a new kind of effective photocatalysts because of their suitable bandgap and high separation rate of photogenerated electrons and holes. In 2015, Li et al.^[46] adopted a simple solvothermal method to synthesize BiOBr nanosheets with abundant OVs exposed on the {001} facet (BOB-001-OV), and observed apparent photocatalytic activity toward nitrogen fixation even under visible light irradiation ($\lambda > 420$ nm), with the amount of NH₃ produced quantified by the Nessler reagent. This was a breakthrough in photocatalytic nitrogen fixation by semiconductor materials. However, with its 2D sheet-like structure and small specific surface area, the nitrogen fixation performance of BOB-001-OV was limited. In a later study in 2017,^[52] Wang et al. successfully synthesized 1D ultrafine Bi₅O₇Br nanotubes by a water-guided self-assembly method, which greatly increased the specific surface area, improved the nitrogen fixation performance, and broke the bottleneck that limited the performance of the 2D counterparts.

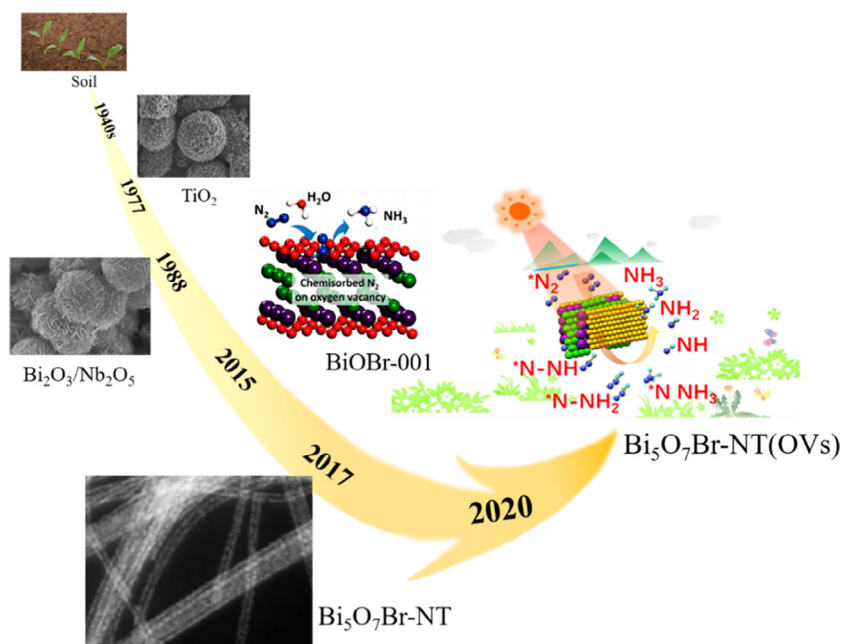


Figure 1. Photocatalytic nitrogen fixation by BiOX materials. Reproduced with permission.^[46] Copyright 2015, American Chemical Society. Reproduced with permission.^[52] Copyright 2017, John Wiley & Sons. Reproduced with permission.^[60] Copyright 2020, American Chemical Society.

Importantly, such a performance can be further enhanced by an increase in surface OV, as demonstrated in a more recent study by Li et al.^[60]

It should be noted that it is the strong interaction between the Bi 6p electrons and N 2p electrons that facilitates the adsorption of N₂ molecules onto the surface of the Bi-based catalysts, especially those with OVs. OVs can accumulate photogenerated electrons on the catalyst surface, which is conducive to N₂ adsorption. This leads to a weakened N≡N bond,^[61] and the resulting activation of N₂ is crucial to the eventual reduction to NH₃.^[22]

2.1. Bismuth Oxyhalides

Because of their unique crystal and electronic structures, bismuth-based oxyhalides exhibit interesting photocatalytic activity and stability, and have been used as effective catalysts for N₂ fixation.^[62] As shown in **Figure 2**, BiOX displays a layer structure consisting of a [Bi₂O₂] plane and two planes of halogen atoms, and belongs to the tetragonal system. The formation of such a layered structure is due to strong covalent bonding interactions within the [Bi₂O₂] layers and superposition of weak van der Waals forces (nonbond interactions) between the X atoms of the [X] layers along the C axis.^[63,64] Importantly, the Bi–O bond has a much lower bond energy and a much longer bond length than other metal–oxygen bonds, which renders it easy to break the Bi–O bond, and for O₂ to escape from the catalyst surface creating OVs.^[46] Notably, whereas the weak interaction between the surface of bismuth oxyhalide and N₂ molecules makes it difficult for N₂ to be chemically adsorbed, the OVs generated by the cleavage of the Bi–O bond greatly facilitate the adsorption of N₂ and increase the yield of N₂ conversion to NH₃.^[22]

In typical metal oxide photocatalysts, the valence band (VB) usually consists of the O 2p orbital. However, for bismuth oxyhalides, both the O 2p and X np (*n* = 3, 4, and 5) orbitals contribute to the VB, whereas the conduction band (CB) is dominated by the Bi 6p orbital.^[47,65] This suggests that X can be exploited as a unique variable for the manipulation of the materials bandgap and therefore the photo absorption range. Note that the bandgap of the BiOX compounds decreases with increasing atomic number of the halogen (**Figure 3a,b**),^[66,67] in the order of BiOCl (3.50 eV) > BiOBr (2.88 eV) > BiOI (1.79 eV).^[67,68] In addition, one can see from Figure 3a that the CB is situated at –1.10 eV for BiOCl, –0.53 eV for BiOBr, and +0.60 eV for BiOI, in comparison to the reduction potential (–0.28 eV) of N₂/NH₃. This suggests that both BiOCl and BiOBr are photocatalytically active toward the reduction of N₂ to NH₃, and BiOBr is the optimal catalyst among the series for nitrogen fixation (whereas the pristine form is inactive, doped and/or defective BiOI also exhibits apparent photocatalytic activity toward nitrogen fixation, vide infra).

The photocatalytic activity toward nitrogen fixation can be further manipulated by the elemental composition of BiOX. For instance, Bi-rich Bi_aO_bX_c has stood out as a unique family of photocatalysts, which also exhibit a layered structure, again, due to strong intralayer bonding and weak interlayer nonbonding (van der Waals force) interactions.^[69] These include Bi_aO_bCl_c (e.g., Bi₂₄O₃₁Cl₁₀, Bi₃O₄Cl, Bi₅O₇Cl, and Bi₁₂O₁₇Cl₂₁), Bi_aO_bBr_c (e.g., Bi₄O₅Br₂, Bi₂₄O₃₁Br₁₀, Bi₃O₄Br, Bi₅O₇Br, and Bi₁₂O₁₇Br₂), and Bi_aO_bI_c (e.g., Bi₄O₅I₂ and Bi₅O₇I). Bi₃O₄Cl is taken as an example and shown in Figure 3c,^[70] where [Bi–O] layers are sandwiched between two layers of chloride ions, forming a self-induced electric field, similar to BiOCl.^[71] Experimentally, the unique band structures of these Bi-rich

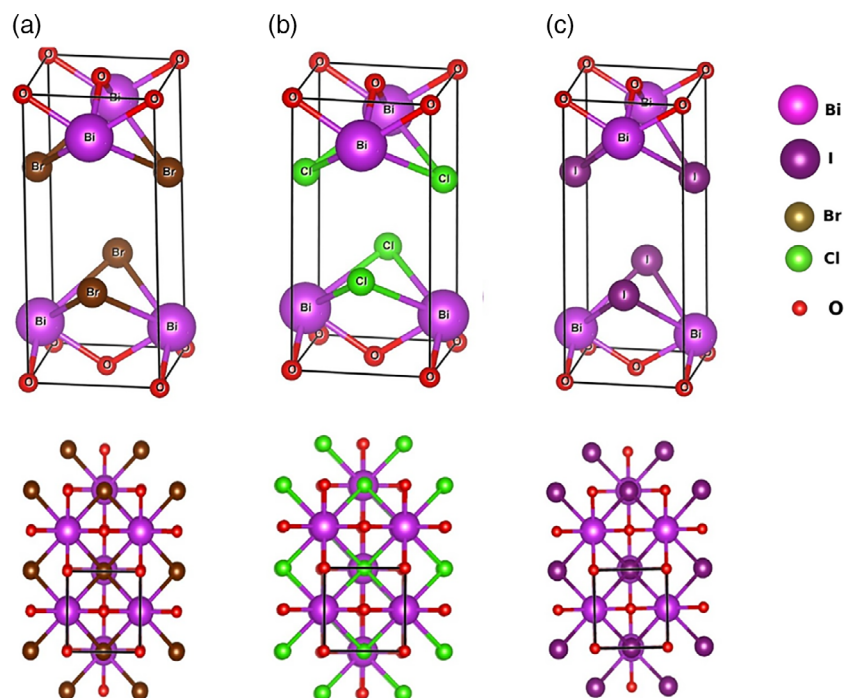


Figure 2. Unit cell of bulk BiOX: a) BiOBr, b) BiOCl, and c) BiOI. The magenta, red, brown, green, and violet balls represent bismuth, oxygen, bromine, chlorine, and iodine atoms, respectively. Reproduced with permission.^[63] Copyright 2020, Elsevier.

materials are found to be conducive for effective photocatalytic nitrogen fixation (Figure 3a).^[72] Specifically, in $\text{Bi}_a\text{O}_b\text{Cl}_c$ and $\text{Bi}_a\text{O}_b\text{Br}_c$, the higher Bi content results in a downward shift of the CB minimum and an upward shift of the VB maximum edge, and therefore, a narrower bandgap than that of BiOCl and BiOBr, whereas a wider bandgap is observed with $\text{Bi}_a\text{O}_b\text{I}_c$ than with BiOI.^[73,74]

The internal electric field (IEF) may also contribute to the photocatalytic activity.^[64] Since the layered crystal structure provides an open space to polarize related atoms and orbitals, the IEF is induced perpendicular to the $[\text{Bi}_2\text{O}_2]$ plane and the halogen anion planes in BiOX (Figure 2). Such an inherent IEF can improve the diffusion of electron–hole pairs, thereby increasing the carrier mobility and reducing the recombination rate, which leads to improved efficiency of photocatalytic nitrogen fixation.^[48,60,75] For instance, Li et al.^[70] demonstrated that manipulation of the IEF amplitude can be exploited as a strategy to improve the activity of the photocatalysts. They prepared single crystal $\text{Bi}_3\text{O}_4\text{Cl}$ nanosheets with rich {001} plane exposure (Figure 3d). When the $\text{Bi}_3\text{O}_4\text{Cl}$ nanosheets were under visible light photoirradiation, electrons were excited from the VB to CB, leaving holes in the VB. The polarization-induced IEF along the {001} crystal orientation of the nanosheets was found to promote the charge separation and facilitate the transfer of charge carriers from the bulk to the surface for subsequent photocatalytic reactions. Thus, an increasing amount of the {001} facet exposure led to improved separation and transfer efficiency of photogenerated electron–hole pairs and eventual photocatalytic activity, due to an enhanced IEF.

2.2. Preparation of Bismuth Oxyhalides

As shown in **Table 1**, a range of methods have been reported for the preparation of BiOX,^[7,8,47,52,60,76–98] which mainly include solvothermal process, precipitation process, reverse microemulsion, low-temperature chemical vapor transport, water guided self-assembly, and so on. The morphologies of the products vary accordingly, including nanospheres, nanowires, nanotubes, nanosheets, and other 2D and 3D nanostructures.

Chemical precipitation method has been widely used for the synthesis of BiOX photocatalysts due to its simple synthetic conditions, high efficiency, and low energy consumption.^[76,77] Li et al. used $\text{Bi}(\text{NO}_3)_3 \cdot 5\text{H}_2\text{O}$ as the bismuth source and KI as the halogen source to successfully synthesize a 3D hierarchical structure composed of BiOI nanoplates by chemical precipitation at room temperature.^[78] The obtained BiOI showed effective photocatalytic activity under visible light for the degradation of model pollutants, such as methyl orange and phenol. Despite the apparent advantages, chemical precipitation also has its shortcomings, such as particle agglomeration, small surface area, impurity formation, uncontrollable morphology, and so on.

Hydrolysis is also a common method for the preparation of BiOX, which is based on the reaction between a Bi salt (e.g., $\text{Bi}(\text{NO}_3)_3$ and BiX_3) and oxyhalide or water.^[48,77,79] The advantage of this method is that BiOX of various sizes can be easily synthesized in a simple reactor. For instance, Wang et al. used a hydrolysis method to prepare ultrafine $\text{Bi}_5\text{O}_7\text{Br}$ nanotubes with a diameter of 5 nm,^[52] which involved two major steps: 1) a bismuth–bromo–oleylamine (Bi–Br–OA) complex was formed by mixing Bi and Br ions in oleylamine and 2) with the gradual

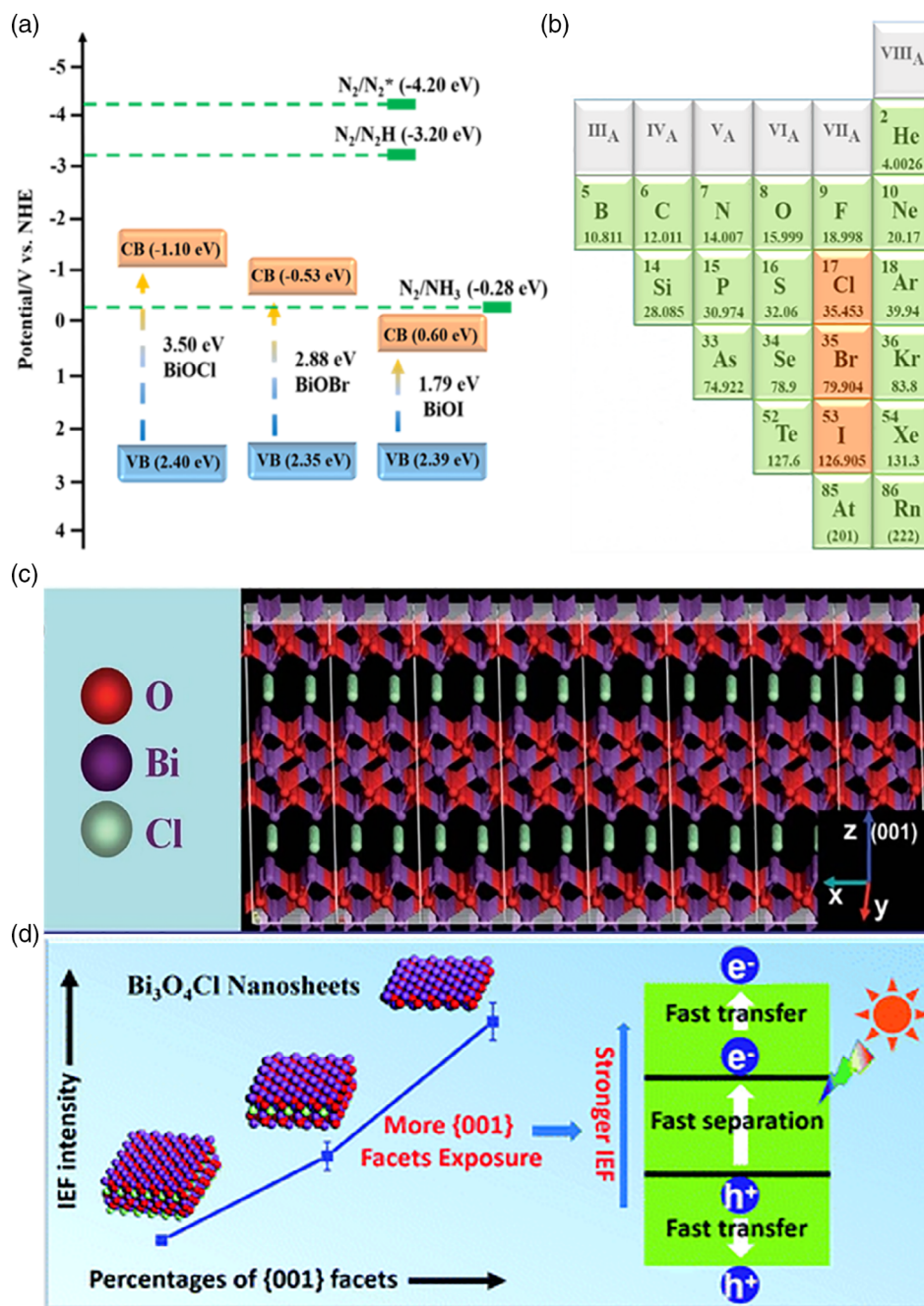


Figure 3. a) Band structures of BiOX. b) Positions of Cl, Br, and I in the periodic table of elements. c) Crystal structure of Bi_3O_4Cl nanosheets. d) Schematic diagram of carrier separation promoted by IEF in Bi_3O_4Cl single crystal nanosheets with high {001} surface exposure. Reproduced with permission.^[70] Copyright 2014, Royal Society of Chemistry.

addition of water, the complex was hydrolyzed producing ultra-fine nanotubes. However, the catalysts synthesized by the hydrolysis method in general have poor dispersibility, and surfactants are usually added to make them dispersible. Therefore, the hydrolysis method is solvent dependent.

In addition to chemical precipitation and hydrolysis, hydrothermal method is also commonly used to synthesize BiOX photocatalysts, where the crystallinity, morphology, and particle size are controllable at low temperatures.^[48,79] A range of

hydrothermal reaction parameters, including reaction duration, temperature, surfactant, precursor concentration, and pH, have been known to play a critical role in defining the physical and chemical properties and ultimately the photocatalytic performance of BiOX. For instance, Jiang et al. successfully synthesized flake-like BiOBr by hydrothermal treatment of $Bi(NO_3)_3 \cdot 5H_2O$ and KBr precursors in acetic acid at 150 °C for 18 h, which showed excellent photocatalytic activity toward the degradation for methyl orange.^[80] Nevertheless, one can see that since the

Table 1. Summary of typical synthesis methods of BiOX in different morphologies.

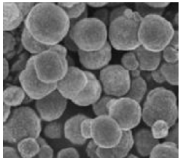
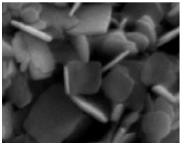
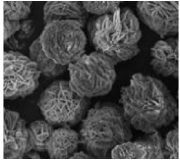
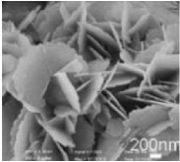
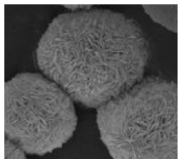
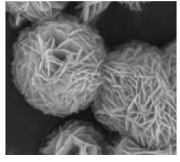
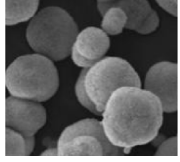
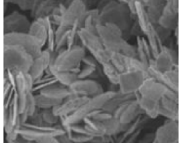
| Synthesis method | Product | Raw materials and synthesis conditions | Material morphology | Ref. |
|----------------------|--|---|---|---|
| Solvothermal process | BiOX | Bi(NO ₃) ₃ ·5H ₂ O, ethylene glycol, KX (X = Cl, Br, I); 160 °C for 12 h. |  | Reproduced with permission. ^[77] Copyright 2013, Royal Society of Chemistry. |
| | | Bi, NaCl, H ₂ O ₂ (36% in v/v); 160–200 °C for 10 h. |  | Reproduced with permission. ^[78] Copyright 2011, Elsevier. |
| BiOCl | Bi(NO ₃) ₃ ·5H ₂ O, KCl, HNO ₃ , PVP; | 180 °C for 18 h |  | Reproduced with permission. ^[81] Copyright 2013, John Wiley & Sons. |
| | | BiCl ₃ , pyridine; 180 °C for 12 h |  | Reproduced with permission. ^[82] Copyright 2010, Royal Society of Chemistry. |
| BiOBr | Bi(NO ₃) ₃ ·5H ₂ O, CTAB, ethylene glycol; | 180 °C for 12 h |  | Reproduced with permission. ^[84] Copyright 2011, Elsevier. |
| | | 150 °C for 24 h |  | Reproduced with permission. ^[85] Copyright 2011, Elsevier. |
| BiOBr | Bi(NO ₃) ₃ ·5H ₂ O, CTAB, ethylene glycol; | 180 °C for 12 h |  | Reproduced with permission. ^[86] Copyright 2008, Elsevier. |
| | | 150 °C for 18 h |  | Reproduced with permission. ^[80] Copyright 2010, Elsevier. |

Table 1. Continued.

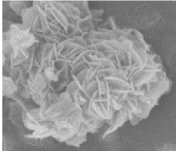


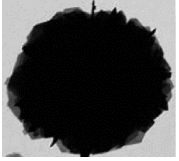
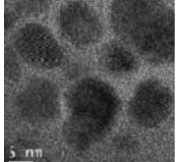
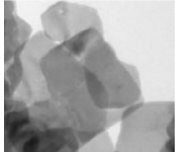
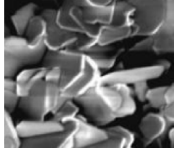
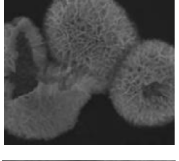
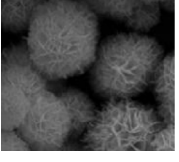
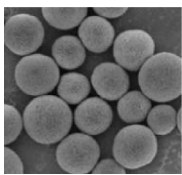
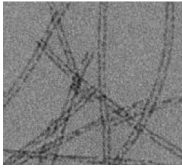
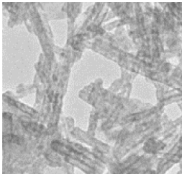
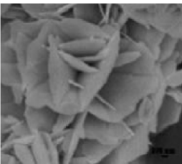
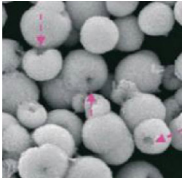
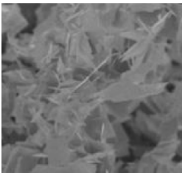
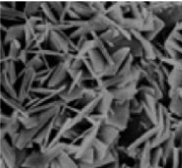
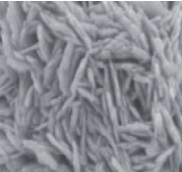
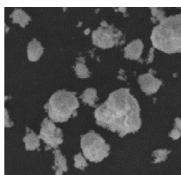
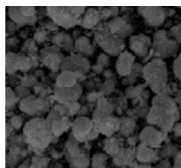
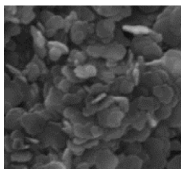
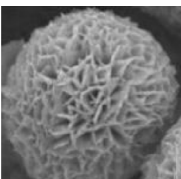
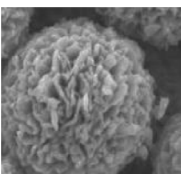
| Synthesis method | Product | Raw materials and synthesis conditions | Material morphology | Ref. |
|--|---|--|---|---|
| C-BiOI | Bi(NO ₃) ₃ ·5H ₂ O, HNO ₃ , glucose, ethanol, 60 °C for 18 h |  | Reproduced with permission. ^[71] Copyright 2019, Elsevier. | |
| Precipitation process | BiOX | NaBiO ₃ ·2H ₂ O, HX (X = Cl, Br, I); room temperature. |  | Reproduced with permission. ^[87] Copyright 2010, Elsevier. |
| | | Bi ₂ O ₃ , HX (X = Cl, Br, I); room temperature. |  | Reproduced with permission. ^[47] Copyright 2008, Springer. |
| BiOI | Bi(NO ₃) ₃ ·5H ₂ O, KI; 80 °C for 3 h; pH = 7 |  | Reproduced with permission. ^[78] Copyright 2011, Elsevier. | |
| Reverse microemulsions | BiOX | Bi(NO ₃) ₃ ·5H ₂ O, KX (X = Cl, Br, I), Marlophen NPS; room temperature. |  | Reproduced with permission. ^[88] Copyright 2007, American Chemical Society. |
| Molecular precursor route | BiOCl | BiCl ₃ , thiourea; room temperature; pH = 4 |  | Reproduced with permission. ^[89] Copyright 2011, Royal Society of Chemistry. |
| Low-temperature chemical vapor transport | BiOCl | BiCl ₃ ; 250 °C |  | Reproduced with permission. ^[90] Copyright 2012, Springer. |
| Miniemulsion-mediated route | BiOBr | Bi(NO ₃) ₃ ·5H ₂ O, ([C16Mim]Br), 2-methoxyethanol; 160 °C for 0.5–24 h |  | Reproduced with permission. ^[91] Copyright 2011, John Wiley & Sons. |
| Isonothermal synthesis | BiOBr | Bi(NO ₃) ₃ ·5H ₂ O, 1-butyl-3-methylimidazolium bromide; 200 °C for 24 h |  | Reproduced with permission. ^[84] Copyright 2011, Elsevier. |

Table 1. Continued.

| Synthesis method | Product | Raw materials and synthesis conditions | Material morphology | Ref. |
|---|---------------------------------------|---|---|---|
| Microwave irradiation process | BiOBr | $\text{Bi}(\text{NO}_3)_3 \cdot 5\text{H}_2\text{O}$, CTAB, diethylene glycol; 180 °C for 10 min |  | Reproduced with permission. ^[92] Copyright 2011, Elsevier. |
| Water-guided self assembly | $\text{Bi}_5\text{O}_7\text{Br}$ | $\text{Bi}(\text{NO}_3)_3 \cdot 5\text{H}_2\text{O}$, KBr, Oleamine, H_2O 25 °C |  | Reproduced with permission. ^[52] Copyright 2017, John Wiley & Sons. |
| Water-guided self assembly + water bath heating | $\text{Bi}_5\text{O}_7\text{Br}$ -OVs | $\text{Bi}(\text{NO}_3)_3 \cdot 5\text{H}_2\text{O}$, KBr, oleylamine, H_2O , 20 °C, 40 °C, 60 °C, 80 °C, 100 °C |  | Reproduced with permission. ^[60] Copyright 2020, American Chemical Society. |
| Ionic liquid modified precipitate process | BiOI | $\text{Bi}(\text{NO}_3)_3 \cdot 5\text{H}_2\text{O}$, [Bmim] ⁺ ; 70 °C for 0.5 h |  | Reproduced with permission. ^[93] Copyright 2004, Elsevier. |
| Ionic liquid modified solvothermal process | BiOI | $\text{Bi}(\text{NO}_3)_3 \cdot 5\text{H}_2\text{O}$, [Bmim] ⁺ ; 140 °C for 24 h |  | Reproduced with permission. ^[94] Copyright 2011, American Chemical Society. |
| Calcination process | BiOI | BiI_3 ; 250 °C for 3 h |  | Reproduced with permission. ^[95] Copyright 2011, Royal Society of Chemistry. |
| | BiOCl | BiCl_3 ; 400 °C for 2 h |  | Reproduced with permission. ^[90] Copyright 2012, Springer. |
| Low-temperature hydrogen annealing + solvothermal process | H-BiOBr | $\text{Bi}(\text{NO}_3)_3 \cdot 5\text{H}_2\text{O}$, NaBr, IPA, 433 K for 12 h |  | Reproduced with permission. ^[96] Copyright 2012, American Chemical Society. |

reaction can be impacted by a number of experimental parameters, it is tedious to identify optimal reaction conditions.^[79]

Table 1. Continued.

| Synthesis method | Product | Raw materials and synthesis conditions | Material morphology | Ref. |
|---|--------------------------------------|---|---|--|
| Molecular precursor method + hydrolytic process | $\text{Bi}_5\text{O}_7\text{I}$ | $\text{Bi}(\text{NO}_3)_3 \cdot 5\text{H}_2\text{O}$, glycerol, 160 °C for 17 h |  | Reproduced with permission. ^[97] Copyright 2016, Elsevier. |
| Molecular precursor method + calcination process | $\text{Bi}_4\text{O}_5\text{I}_2$ | $\text{Bi}(\text{NO}_3)_3 \cdot 5\text{H}_2\text{O}$, glycerol, 300 °C for 5 h |  | Reproduced with permission. ^[97] Copyright 2016, Elsevier. |
| Hydrolytic process | $\text{Bi}_5\text{O}_7\text{I}$ -100 | $\text{Bi}_5\text{O}_7\text{I}$, 400 °C for 3 h |  | Reproduced with permission. ^[98] Copyright 2016, American Chemical Society. |
| Chemical precipitation method | BiOI | $\text{Bi}(\text{NO}_3)_3 \cdot 5\text{H}_2\text{O}$, KI, ethylene glycol, 60 °C for 4 h |  | Reproduced with permission. ^[8] Copyright 2020, Royal Society of Chemistry. |
| Calcination and H-Bi5O7I hydrogen reduction process | $\text{Bi}_5\text{O}_7\text{I}$ | $\text{Bi}_5\text{O}_7\text{I}$, H_2 , 300 °C for 4 h |  | Reproduced with permission. ^[8] Copyright 2020, Royal Society of Chemistry. |

Such BiOX-based catalysts exhibit apparent photocatalytic activity toward nitrogen fixation.^[99–114] As depicted in **Table 2**, in a previous study, Li et al.^[46] prepared BiOBr nanosheets with abundant OV on the exposed {001} surface and observed a photocatalytic nitrogen fixation rate of $104.2 \mu\text{mol h}^{-1} \text{g}^{-1}$ under visible light photoirradiation. In a later study, Wang et al.^[52] prepared $\text{Bi}_5\text{O}_7\text{Br}$ nanotubes, and observed an improved photocatalytic nitrogen fixation rate of $1.38 \text{ mmol h}^{-1} \text{g}^{-1}$. Bi et al.^[99] found that the visible light nitrogen fixation rate of H-BiOBr (BiOBr hollow microspheres prepared by the same calcination method but in a H_2 atmosphere) can reach $50.8 \mu\text{mol g}^{-1} \text{h}^{-1}$. Di et al.^[100] studied the promotion effect of structural defects in facilitating electron-hole separation in $\text{Bi}_3\text{O}_4\text{Br}$ nanosheets and observed a photocatalytic hydrogen evolution rate of $25.4 \mu\text{mol L}^{-1}$. Liu et al.^[101] reported photocatalytic conversion of nitrogen and water to ammonia at the $\text{Bi}_4\text{O}_5\text{Br}_2/\text{ZIF-8}$ three-phase interface at a rate of $327 \mu\text{mol L}^{-1} \text{h}^{-1} \text{g}^{-1}$. In addition, Li et al.^[60] showed that the nitrogen fixation rate of $\text{Bi}_5\text{O}_7\text{Br}$ can be increased to $12.72 \text{ mmol g}^{-1} \text{h}^{-1}$ by an increase in the OV concentration. The application of BiOCl in photocatalytic nitrogen fixation was first reported in 2016 by Li et al.,^[102] where

Table 2. Studies on photocatalytic reduction of nitrogen over BiOX photocatalysts.

| Catalysts | Conditions | Yield | AQE [%] | Stability [cycle] | Ref. |
|--|--|--|-------------------|-------------------|-----------|
| BiOBr, exposed {001} facets | 300 W Xenon lamp ($\lambda > 420$ nm), 25 °C | 104.2 $\mu\text{mol h}^{-1} \text{g}^{-1}$ | / | 7 | [46] |
| Bi ₅ O ₇ I | 300 W Xenon lamp (280–800 nm), 20 °C | 111.5 $\mu\text{mol L}^{-1} \text{h}^{-1}$ | 5.1/1.6 at 365 nm | 5 | [97] |
| BiOCl | 500 W Xenon lamp 25 °C | 4.62 $\mu\text{mol h}^{-1}$ | 4.3 at 254 nm | 5 | [102] |
| Bi ₅ O ₇ Br, H ₂ O | 300 W Xe lamp $\lambda > 400$ nm, 25 °C | 1.38 mmol h ⁻¹ g ⁻¹ | 2.3 at 420 nm | 4 | [52] |
| H-BiOBr | 300 W Xenon lamp (300–600 nm) 25 °C | 50.8 $\mu\text{mol g}^{-1} \text{h}^{-1}$, | 2.1 at 380 nm | 5 | [99] |
| Bi ₂ Te ₃ /BiOCl | 25 °C | 315.9 $\mu\text{mol L}^{-1} \text{h}^{-1}$ | / | 5 | [68] |
| C-BiOI | 300 W xenon lamp | 311 $\mu\text{mol g}^{-1} \text{h}^{-1}$ | / | 6 | [5] |
| Bi ₃ O ₄ Br | 300 W xenon lamp 30 °C | 25.4 $\mu\text{mol L}^{-1}$ | 1.59 at 400 nm | 4 | [100] |
| BiOI | (200–800 nm), 25 °C | 83 $\mu\text{mol L}^{-1} \text{g}^{-1} \text{h}^{-1}$ | / | 6 | [5] |
| BiOCl–OV | 300 W Xe lamp, 25 °C | 6.3 $\mu\text{mol h}^{-1}$ | / | 5 | [103] |
| 2D/2D ZnIn ₂ S ₄ /BiOCl heterostructure | 300 W Xe lamp (200–800 nm) 25 °C | 14.6 $\mu\text{mol g}^{-1} \text{h}^{-1}$ | / | 5 | [67] |
| Bi ₄ O ₅ Br ₂ /ZIF-8 | (300–700 nm) 25 °C | 327.338 $\mu\text{mol L}^{-1} \text{h}^{-1} \text{g}^{-1}$ | / | 5 | [101] |
| Bi ₂ MoO ₆ /OV–BiOBr heterojunctions | 300 W xenon lamp 25 °C | 90.7 $\mu\text{mol g}^{-1} \text{h}^{-1}$ | / | 6 | [53] |
| Bi ₂ S ₃ /BiOBr hybrid | 300 W Xe lamp cutoff filter ($\lambda > 420$ nm) | 878 $\mu\text{mol g}^{-1}$ | / | 4 | [113,114] |
| Bi ₅ O ₇ Br-40 | 300 W xenon lamp (200–800 nm), 25 °C | 12.72 mmol g ⁻¹ h ⁻¹ | / | 5 | [60] |
| H-Bi ₅ O ₇ I microspheres | 300 W xenon lamp, 25 °C | 162.48 $\mu\text{mol g}^{-1} \text{h}^{-1}$ | / | 4 | [8] |

BiOCl nanosheets were synthesized and involved in the proton-assisted electron-transfer pathway. Rong et al.^[68] reported the application of Bi₂Te₃/BiOCl in photocatalytic nitrogen fixation in 2018, with a nitrogen fixation rate of 315.9 $\mu\text{mol L}^{-1} \text{h}^{-1}$. Guo et al.^[67] prepared a 2D/2D ZnIn₂S₄/BiOCl heterostructure for N₂ fixation at a rate of 14.6 $\mu\text{mol g}^{-1} \text{h}^{-1}$. Wu et al.^[103] reported that the abundant OVs and dominant {001} surface of Br-doped porous BiOCl microchips led to an improved performance of nitrogen fixation. Doped/defective BiOI has also been used for photocatalytic nitrogen fixation. In 2019, Zeng et al.^[5] reported the preparation of interstitial carbon-doped BiOI, which exhibited a photocatalytic nitrogen fixation rate of 311 $\mu\text{mol g}^{-1} \text{h}^{-1}$. In 2020, Lan et al.^[8] prepared H-Bi₅O₇I microspheres with rich OVs for visible light nitrogen fixation, and observed a rate of 162.48 $\mu\text{mol g}^{-1} \text{h}^{-1}$.

In general, the apparent quantum efficiency (AQE) of photocatalytic nitrogen fixation is low under ambient temperature and pressure. As shown in Table 2, Wang et al.^[52] synthesized Bi₅O₇Br nanotubes and observed an AQE of only 2.3% at 420 nm, the highest ever reported. But, this is still far lower than actual industrial application requirements.^[104] Nevertheless, such bismuth oxyhalides have been found to exhibit good stability and reusability (Table 2).

Notably, the formation of OVs in BiOX facilitates oxygen production,^[105] nitrogen fixation,^[1,52,106] CO₂ reduction,^[107,108] and organic pollutant degradations.^[108,109] Despite the apparent advantages, limitations of the photocatalytic performance of BiOX remain, such as relatively large bandgaps that limit the solar light utilization efficiency, high recombination of

photogenerated electron-hole pairs, and limited surface active centers. Further structural engineering is needed to optimize the performance, as detailed below.

2.3. Sacrificial Agents and Nitrogen Sources

Solar ammonia synthesis is usually conducted in two ways. The first is in ultrapure water,^[46,52,60] and the other is in the presence of sacrificial agents (such as methanol, ethanol, or isopropanol) in water.^[31,98,110] In the latter, a sacrificial agent is added to the photocatalytic reaction system (aqueous solution) to consume photogenerated holes and prevent photogenerated electrons from recombining with holes. For instance, Gao et al.^[111] used the Nessler method and cation exchange chromatography (CEC) to quantify and compare ammonia production with and without sacrificial agents. For alcohol sacrificial agents, they may be oxidized into carbonyl-containing compounds, such as aldehydes and ketones, and form complexes with NH₃, leading to an increase in the absorbance of the Nessler reagent. As the amount of ammonia produced in the traditional photocatalytic ammonia production experiment is extremely small (100–1000 $\mu\text{mol g}^{-1} \text{h}^{-1}$, Table 2), the coexistence of sacrificial agents and the Nessler reagent may compromise the rationality and accuracy of the positive detection of ammonia production. By contrast, CEC is far more reliable and accurate, as these organic compounds do not interfere with CEC analysis.^[111]

Furthermore, in recent years, tracking the source of nitrogen in ammonia production has also been the focus of extensive

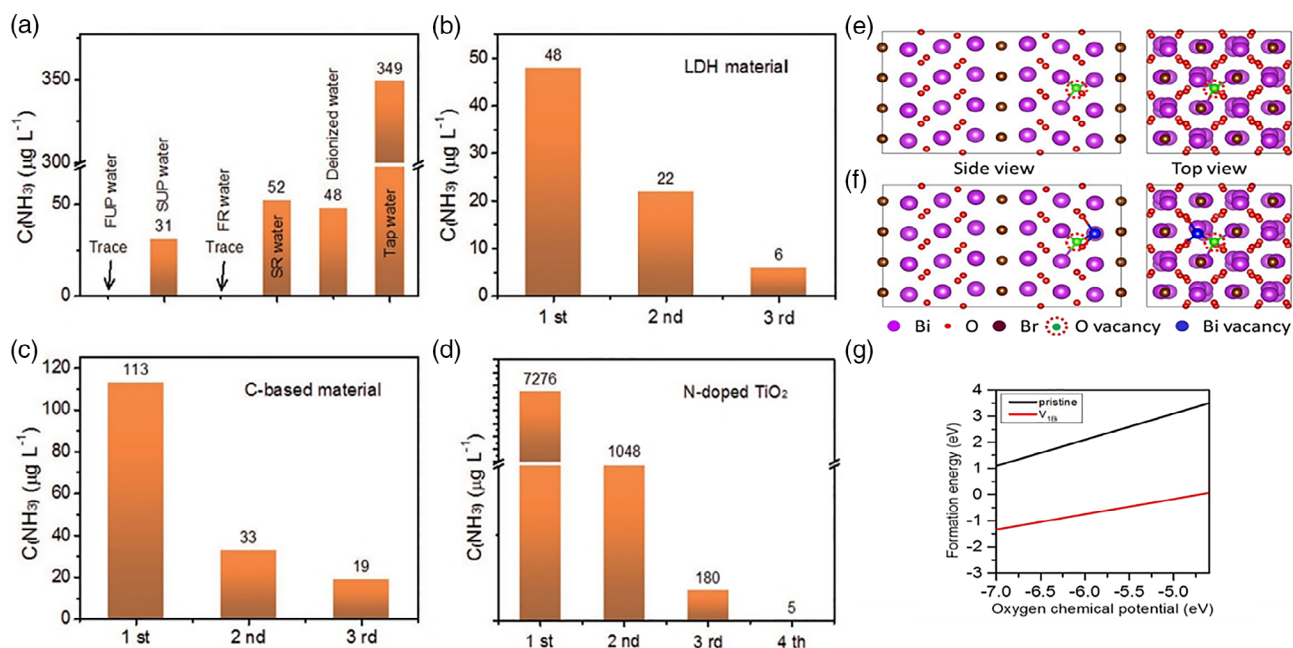


Figure 4. Ammonia concentration determined by ion chromatography with a) different types of water (FUP is fresh ultrapure water, SUP is stale ultrapure water, FR is fresh redistilled water, and SR is stale redistilled water) and b–d) aqueous solutions containing LDH, C-based materials, and N-doped materials before and after washing with ultrapure water. Reproduced with permission.^[112] Copyright 2019, John Wiley & Sons. OV formed in e) pristine $\text{Bi}_3\text{O}_4\text{Br}$ and f) $\text{Bi}_3\text{O}_4\text{Br}$ with one bismuth vacancy. The calculated results of OV formation energy is shown in g), where bismuth vacancy can greatly reduce the OV formation energy. Reproduced with permission.^[100] Copyright 2019, John Wiley & Sons.

studies. Strict experimental protocols need to be followed to ensure the credibility of the results and minimize pollution of the photocatalysts. For instance, Zhang et al.^[112] found that the ammonia concentration in tap water ($349 \mu\text{g L}^{-1}$) was actually much higher than that of stale ultrapure water ($31 \mu\text{g L}^{-1}$), stale redistilled water ($52 \mu\text{g L}^{-1}$), and deionized water ($48 \mu\text{g L}^{-1}$) (Figure 4a), whereas no ammonia was detected in fresh ultrapure water or fresh redistilled water. Thus, fresh ultrapure water or fresh redistilled water must be used in the photocatalytic experiments. In addition, prior to actual reactions, ammonia or amino groups may chemisorb or physisorb onto the photocatalyst surface, and such pollution may lead to interference with the detection of ammonia, and promote reactions that would not otherwise occur on the surface of clean catalysts, as observed with a series of photocatalysts (Figure 4b–d). Note that adsorbed ammonia can be easily removed within five washing cycles. Therefore, before the catalyst is loaded into the aqueous reaction, it should be rinsed with fresh ultrapure water until no ammonium is detected. In addition, it is recommended to conduct a control experiment in the presence of Ar and $^{15}\text{N}_2$ to prove that NH_3 is indeed produced from the provided N_2 rather than from other contaminations (e.g., air, gloves, chemical reagents, glasswares, etc).

3. Mechanism of Nitrogen Fixation

Through the analysis of OVs and different nitrogen fixation pathways, the mechanism of photocatalytic nitrogen fixation is rationalized and summarized in the following section.

3.1. Role of OVs

OVs can be produced by oxygen detachment from the surfaces of transition metal oxides, affect the materials physical and chemical properties with undercoordinated atoms, and promote the formation of catalytic active sites.^[51,115] In photocatalytic nitrogen fixation, one major challenge is the adsorption and activation of inert nitrogen molecules under ambient conditions.^[73,116] This can be facilitated by surface OVs. In fact, vacancies or defects on the surface of photocatalysts can act as trapping sites for photogenerated electrons or protons to inhibit charge recombination,^[117,118] and the surviving charges can participate in the adsorption of important reaction intermediates and boost the photocatalytic performance.^[107] Note that the residual electrons are usually selectively localized near the Bi atoms around the OVs, rather than uniformly distributed in the entire crystal, leading to the coexistence of OVs and low-valence Bi. Thus, the OVs on the BiOX surface can serve as active sites for nitrogen fixation, where molecular nitrogen is adsorbed and activated, and photogenerated electrons are transferred to the surface OVs to achieve efficient nitrogen reduction. In addition, in the band structure, the impurity energy level composed of Bi p orbital and O p orbital typically appears below the bottom of the CB, which inhibits the recombination of photogenerated electrons and holes.^[46] Indeed, extensively studies have shown that the OVs in oxide-based photocatalysts directly affect the nitrogen fixation efficiency.^[119]

In an early study, Di et al.^[100] calculated the formation energy of OVs by using two models, one with a Bi atom defect and the other without a Bi atom defect. It was found that the Bi

atom defect can effectively reduce the oxygen hole formation energy, so that oxygen-rich materials can be easily obtained (Figure 4e–g).^[120] On the basis of these calculations, it was argued that by controlling the surface bismuth defect concentration, a tunable OV can be achieved to tailor the electronic structure of $\text{Bi}_3\text{O}_4\text{Br}$ and serve as surface charge separation centers to further promote the photocatalytic activity.^[5,73]

In another study, Lan et al.^[8] reported that the abundant OVs in bismuth-rich BiOI microspheres contributed to efficient nitrogen fixation under visible light irradiation. Experimentally, the $\text{Bi}_5\text{O}_7\text{I}$ powders were annealed in a H_2 atmosphere at 300°C for 4 h to produce hydrogenated $\text{Bi}_5\text{O}_7\text{I}$ (denoted as $\text{H-Bi}_5\text{O}_7\text{I}$). Both $\text{Bi}_5\text{O}_7\text{I}$ and $\text{H-Bi}_5\text{O}_7\text{I}$ displayed electron paramagnetic resonance (EPR) signals at $g = 2.0$ (Figure 5a), suggesting the formation of OVs, and the OV concentration was higher in $\text{H-Bi}_5\text{O}_7\text{I}$ than in $\text{Bi}_5\text{O}_7\text{I}$. This is likely because a large number of oxygen atoms were detached from the $\text{Bi}_5\text{O}_7\text{I}$ surface during hydrogenation.^[46,120,121] In photocatalytic nitrogen fixation tests (Figure 5b), a large amount of NH_3 was produced with $\text{H-Bi}_5\text{O}_7\text{I}$ after 180 min of visible light irradiation at a nitrogen fixation rate of $162.48 \mu\text{mol g}^{-1} \text{h}^{-1}$, and the amount of NH_3 produced increased approximately linearly with the illumination time. Such a performance was markedly better than that of pristine $\text{Bi}_5\text{O}_7\text{I}$, suggesting the significant role of OVs in the adsorption and activation of N_2 molecules. Notably, the OVs can also impede the recombination of charge carriers and facilitate interfacial charge transfer from the semiconductor to N_2 . In addition, $\text{H-Bi}_5\text{O}_7\text{I}$ exhibited excellent stability in nitrogen fixation (Figure 5c), where no significant attenuation of the photocatalytic

activity was observed even after four cycles, and no obvious change was detected in X-ray diffraction (XRD) measurements of the used $\text{H-Bi}_5\text{O}_7\text{I}$ sample (Figure 5d).

In another study, Li et al.^[60] examined the effect of OV concentration on the performance of visible light-driven nitrogen fixation catalyzed by $\text{Bi}_5\text{O}_7\text{Br}$ nanostructures. Density functional theory (DFT) calculations were conducted to evaluate the Gibbs free energy of each reaction step on pristine $\text{Bi}_5\text{O}_7\text{Br}$, oxygen-rare $\text{Bi}_5\text{O}_7\text{Br-O}$, and oxygen-rich $\text{Bi}_5\text{O}_7\text{Br+O}$ (Figure 6a). The corresponding N_2 adsorption energies were also calculated. From the reaction energy diagram, a nitrogen fixation pathway was proposed, $^*\text{N}_2 \rightarrow ^*\text{NNH} \rightarrow ^*\text{NNH}_2 \rightarrow ^*\text{NNH}_3 \rightarrow ^*\text{N} + \text{NH}_3 \rightarrow ^*\text{NH} \rightarrow ^*\text{NH}_2 \rightarrow ^*\text{NH}_3 \rightarrow \text{NH}_3$ (Figure 6b and c), where one can see that N_2 adsorption on $\text{Bi}_5\text{O}_7\text{Br-O}$ was indeed favored with the most negative adsorption free energy (-0.017 eV) for the initial N_2 activation ($^*\text{N}_2$), in comparison to -0.008 eV for pristine $\text{Bi}_5\text{O}_7\text{Br}$ and -0.001 eV for $\text{Bi}_5\text{O}_7\text{Br+O}$ (Figure 6d). The $^*\text{N} - \text{NH}_2 \rightarrow ^*\text{N} - \text{NH}_3$ step exhibits the highest energy barrier (Figure 6b), suggesting that this is the rate-determining step in this reaction pathway.^[122] It can be confirmed from these calculations that OVs indeed play an important role in determining the nitrogen fixation performance. The higher the OV concentration, the more favorable the reduction of N_2 to NH_3 .^[123]

3.2. Mechanism and Pathways of Nitrogen Fixation

As shown in Figure 7a, the catalytic activity of semiconductor photocatalysts arises from photogenerated carriers (i.e., electron–hole pairs),^[124,125] where holes reside in the VB and electrons in

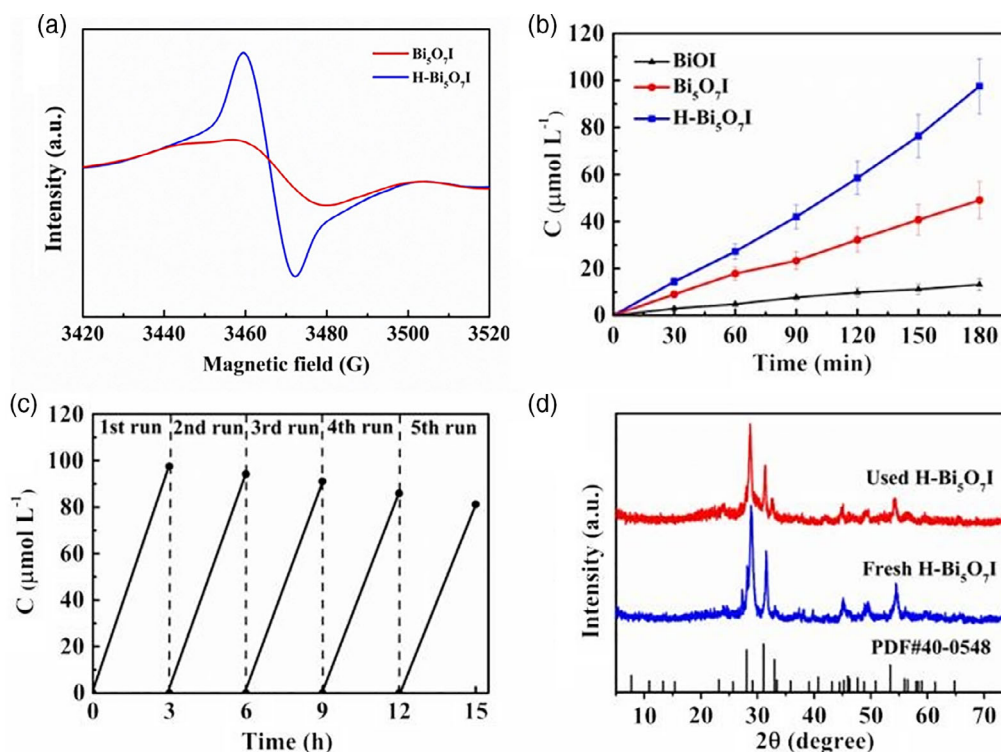


Figure 5. a) EPR spectra of OVs in $\text{Bi}_5\text{O}_7\text{I}$ and $\text{H-Bi}_5\text{O}_7\text{I}$. b) Photocatalytic NH_3 generation under N_2 . c) Cyclic experiment of $\text{H-Bi}_5\text{O}_7\text{I}$. d) XRD patterns of fresh and used $\text{H-Bi}_5\text{O}_7\text{I}$. Reproduced with permission.^[8] Copyright 2020, Royal Society of Chemistry.

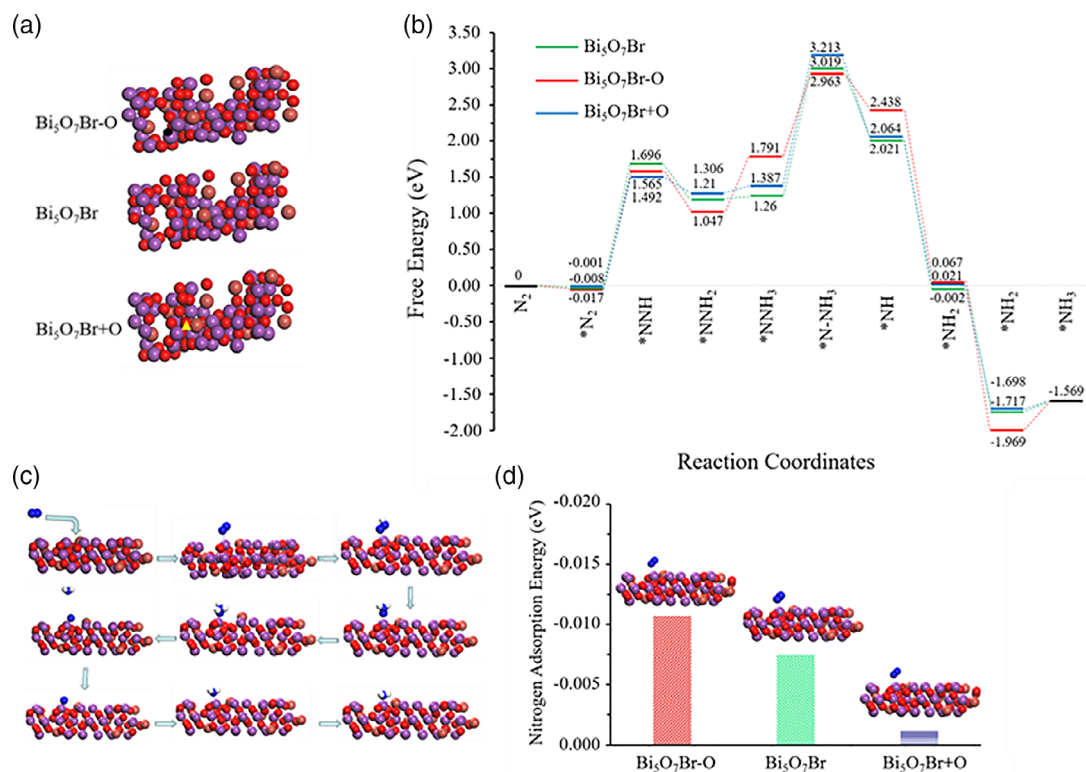


Figure 6. a) Structural models of anoxic Bi₅O₇Br-O, pristine Bi₅O₇Br, and oxygen-enriched Bi₅O₇Br (Bi₅O₇Br+O). The black circle represents the site of an OV, and the yellow triangle refers to the site of the additional oxygen. b) Reaction energy diagram of nitrogen fixation catalyzed by Bi₅O₇Br-O, Bi₅O₇Br, and Bi₅O₇Br+O. c) Schematic pathway of nitrogen fixation. d) Nitrogen adsorption energy on the surfaces of Bi₅O₇Br-O, Bi₅O₇Br, and Bi₅O₇Br+O. Reproduced with permission.^[60] Copyright 2020, American Chemical Society.

the CB.^[126] Migration of these carriers to the catalyst surface renders it possible to undergo redox reactions with N₂, H₂O, etc.^[127] Therefore, the mechanism of photocatalytic nitrogen fixation is similar to that of water decomposition and CO₂ reduction.^[128] First, some oxygen atoms on the catalyst surface are separated from the holes by photoirradiation, forming oxygen holes at the top of the VB^[129]; concurrently, the electrons become excited to the CB.^[130] When N₂ and H₂O molecules are adsorbed to the holes, the N≡N bond and H–O bond become activated and broken by the photogenerated electrons, reducing N₂ to NH₃.^[131] In this reaction, H₂O loses electrons on the VB and is oxidized to form O₂ and H⁺, and N₂ and protons accept electrons on the CB to produce NH₃.^[100,132]

Note that nitrogen adsorption is facilitated by the formation of σ and π bonds by the d orbitals of transition metals and p orbitals of N₂. The π back bonding from the transition metals to N₂ weakens the N≡N triple bond and enhances the strength of metal–N bond.^[133] In addition, DFT calculations show that the {001} plane OV tends to adsorb N₂ in the end-on configuration, with only a single N atom bonded to two Bi atoms, whereas for OVs on the {010} plane, N₂ adsorption adopts a side-on form, with the two N atoms bonded to three adjacent Bi atoms (Figure 7b–d). In the latter, because of simultaneous adsorption and activation of both N atoms, the N–N bond length was elongated to 1.198 Å from 1.09 Å, in comparison to only 1.137 Å in the former. Thus, the {010} plane OVs are more effective in activating molecular

nitrogen than those on the {001} plane. Consistent results were obtained in the calculations of the energy of N₂ adsorption.^[102]

Figure 7e shows the mechanism of photocatalytic nitrogen fixation by Bi₅O₇Br. Under photo irradiation, the nitrogen fixation reaction on the Bi₅O₇Br surface can be divided into two processes: 1) water splitting and 2) reduction of N₂ to NH₃. In general, catalytic nitrogen fixation at a heterogeneous surface can proceed by two recognized mechanisms: associative mechanism and dissociative mechanism.^[8,119,121,134,135]

Theoretically, the Haber–Bosch process follows the dissociative mechanism (Figure 7f).^[24,136] In this process, NH₃ is formed by the combination of N and H⁺ after the bond breaking of N₂. Because of the high bond energy of N≡N, a significant energy input is required in this initial step.^[137] Two different associative N₂ reduction pathways have been considered, i.e., distal and alternating pathways, invoking distinctly different intermediates. As shown in Figure 7f, in the alternating pathway, two N atoms are hydrogenated alternately, forming hydrazine intermediates after four hydrogenation steps, and only the first NH₃ is released in the fifth step. In comparison, in the distal pathway, a single N atom of N₂ is hydrogenated in three steps until the first NH₃ is released, and then, the remaining nitride-N is hydrogenated three more times to produce a second NH₃.^[138] Protonation tends to take place on the nitrogen atom far away from the catalyst surface in the distal associative mechanism. However, in the alternating pathway, protons are in turn added onto the two

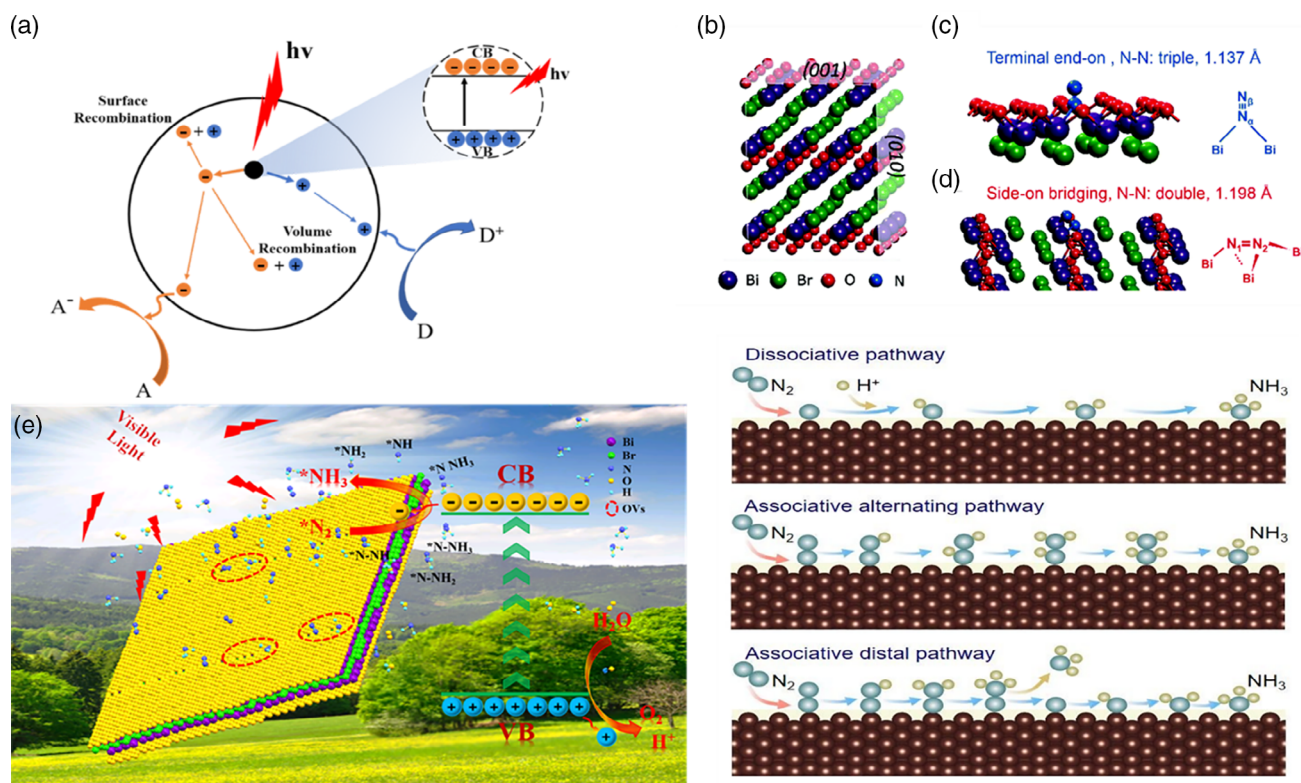


Figure 7. a) Schematic of photoexcitation in a solid followed by deexcitation events. Adsorption of N_2 on the {001} and {010} facets of BiOCl. b) Crystal structure of BiOCl and the corresponding cleaved (001) and (010) surface. c) Terminal end-on adsorption of N_2 on the (001) surface and d) side-on bridging adsorption of N_2 on the (010) surface of BiOCl. Reproduced with permission.^[102] Copyright 2016, Royal Society of Chemistry. e) Schematic diagram of photocatalytic nitrogen fixation catalyzed by Bi_5O_7Br . Reproduced with permission.^[60] Copyright 2020, American Chemical Society. f) Traditionally accepted mechanisms of nitrogen reduction to ammonia. Reproduced with permission.^[24] Copyright 2020, Royal Society of Chemistry.

nitrogen atoms of N_2 before one of the nitrogen atoms is converted into NH_3 by the N–N bond cleavage. However, DFT calculations indicate that the detailed pathways of heterogeneous catalytic nitrogen reduction reaction in aqueous solution vary with the catalytic systems and catalyst materials.^[139]

4. Strategies for Activity Enhancement of BiOX Photocatalysts

As shown earlier, bismuth oxyhalides have been proved to be promising photocatalysts toward N_2 reduction to NH_3 . However, due to the large energy bandgap, most Bi-based photocatalysts exhibit only a low utilization rate of solar energy and a high recombination rate of photoexcited charge carriers, which compromises the photocatalytic nitrogen fixation efficiency.^[5,8,24,140] To mitigate these issues,^[53] a variety of strategies have been developed, such as elemental doping^[141] and formation of heterostructures,^[53,140] whereby the bandgap and electronic structure of the materials can be readily manipulated.

4.1. Elemental Doping

Elemental doping is one of the most important means of structural engineering.^[142] Indeed, a number of studies have

been conducted where doping is used to manipulate the photocatalytic nitrogen fixation performance of BiOX. For instance, Liu et al.^[106] studied the performance of Fe-doped BiOBr in photocatalytic nitrogen fixation. Experimentally, $Bi(NO_3)_3 \cdot 5H_2O$ (1.5 mmol), KBr (1.5 mmol), and a certain amount of $Fe(NO_3)_3 \cdot 9H_2O$ (0, 0.15, 0.3, 0.45, 0.75 and 1.5 mmol) were added to 18 mL of polyethylene alcohol under stirring for 4 h. The mixture was then transferred to a 20 mL Teflon-lined stainless steel autoclave and heated at 160 °C for 10 h. The resulting precipitate was collected by centrifugation. The final product was rinsed with deionized water and ethanol to remove residual ions, and dried in the air at 40 °C to obtain BiOBr and Fe–BiOBr materials. **Figure 8a,b** shows the high-resolution transmission electron microscopy (HRTEM) images of BiOBr and Fe–BiOBr, respectively. From the lattice fringes in **Figure 8a**, the interplanar distance of the BiOBr(101) facets is estimated to be 0.344 nm, which diminishes slightly to 0.340 nm in Fe–BiOBr (**Figure 8b**), suggesting that the incorporation of Fe into BiOBr leads to lattice compression.^[143] Low-temperature electron paramagnetic resonance (EPR) measurements were then conducted to evaluate and compare the OV concentration in Fe–BiOBr, and BiOBr. From **Figure 8c**, one can see that BiOBr exhibits a clearly defined signal at 3400 G with $g = 1.999$ that is characteristic of OVs.^[46,52] After Fe doping, the signal became intensified significantly (Fe–BiOBr), whereas the signal

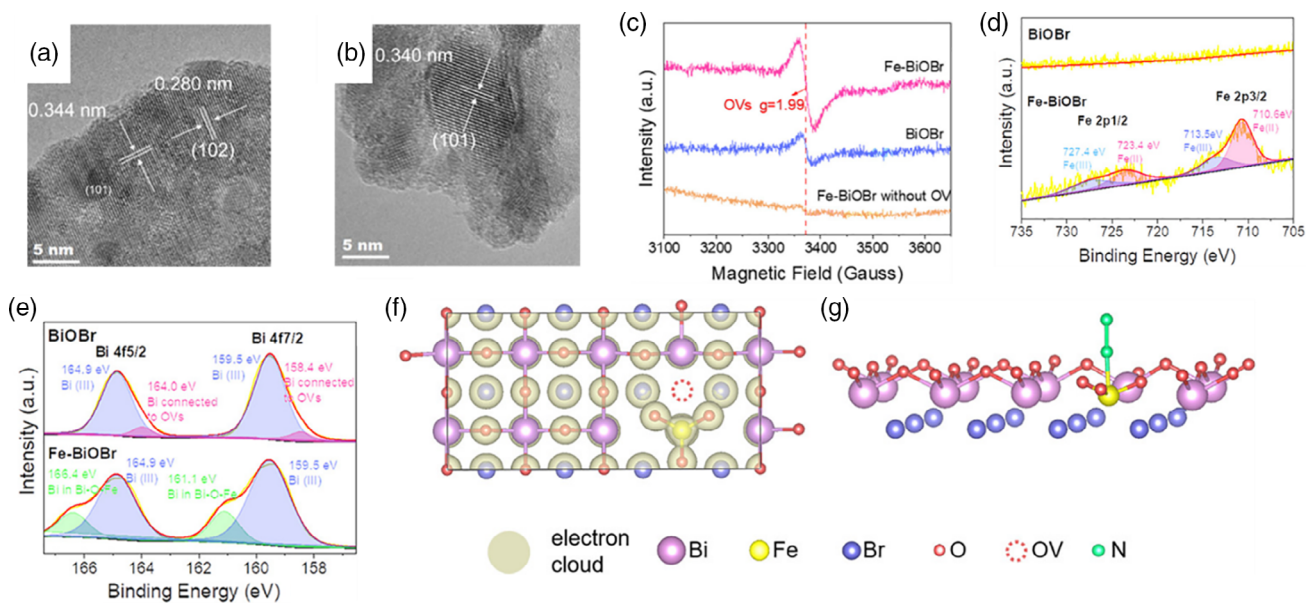


Figure 8. a, b) HRTEM images of BiOBr and Fe-BiOBr. c) EPR spectra of Fe-BiOBr, BiOBr, and OV-free Fe-BiOBr. XPS spectra of the d) Fe 2p and e) Bi 4f electrons in BiOBr and Fe-BiOBr. f) Charge density map of Fe-BiOBr. g) Schematic of N₂ binding to the OV-connected Fe atom in Fe-BiOBr. Reproduced with permission.^[106] Copyright 2020, American Chemical Society.

vanished altogether after the sample was calcined in air at 300 °C for 5 h, suggesting the disappearance of OVs (OV-free Fe-BiOBr). This indicates that Fe doping promoted the generation of OVs on the BiOBr surface.

The material structures were further characterized by X-ray photoelectron spectroscopy (XPS) measurements. In the Fe 2p spectrum of Fe-BiOBr (Figure 8d), two peaks can be resolved at 713.5/727.4 eV and 710.6/723.4 eV, corresponding to the 2p_{3/2} electrons of Fe(III) and Fe(II) species, respectively.^[144] In the Bi 4f spectra of Fe-BiOBr and pristine BiOBr (Figure 8e), two main peaks can be identified at 164.0 eV and 159.5 eV, due to the 4f_{5/2} and 4f_{7/2} electrons of Bi(III), respectively. Two additional peaks are observed in the spectrum of BiOBr at somewhat lower binding energies of 163.8 and 158.4 eV, corresponding to the OV-bound Bi atoms,^[52,145] which have been known to be able to activate the N≡N triple bond.^[52] In the Bi 4f spectrum of Fe-BiOBr, the two additional peaks at the higher binding energies of 166.4 and 161.1 eV are indicative of Bi at a higher valence state,^[146] likely due to electron transfer to Fe through the Bi-O-Fe bond. That is, Fe withdrew electrons from the nearby O and Bi atoms to form electron-rich Fe(II), which is prone to donate the excess electrons to produce more stable half-filled 3d orbitals of Fe(III).^[147] Therefore, the OV-bound Fe(II) atoms in Fe-BiOBr are believed to be the active sites for N₂ photo fixation. Consistent results were obtained in DFT calculations. In the charge density map of Fe-BiOBr (Figure 8f), the electron clouds of the O atoms around Fe are deformed and withdrawn by Fe, and the electron-rich Fe binds with N₂ and activates the triple bond by injecting the localized electrons (Figure 8g).^[148] The N₂ photo fixation efficiency was evaluated under visible light without any sacrificial agent. As shown in Figure 9a, the performance of Fe-BiOBr (382.6 μmol⁻¹ g⁻¹ h⁻¹) was eight times better than that of pristine BiOBr (51.68 μmol⁻¹ g⁻¹ h⁻¹), and there

was virtually no decline of the activity after four cycles of test (Figure 9b).

Similarly, Zhang et al.^[149] used bismuth chloride (BiCl₃) and 2,4-diiron(III) glutarate (Fe(acac)₃) as precursors, polyvinylpyrrolidone (PVP, MW = 58 000) as a surfactant, and glycol as a solvent, and synthesized Fe-doped BiOCl nanosheets (BiOCl NSs-Fe-x%, with x = 1.5, 2.5, 5, 7.5, and 10, representing the initial Fe(acac)₃ feed). One can see from Figure 9c that the BiOCl nanosheets doped with 5% Fe exhibited the maximum NH₃ generation rate of 1.022 mmol g⁻¹ h⁻¹, and long-lasting stability after five cycles (Figure 9d).

In another study, Zeng et al.^[5] dissolved 1.94 g of Bi(NO₃)₃·5H₂O in 40 mL of 1 M HNO₃ under stirring for 30 min. Then, 0.005 g of glucose was added under sonication for 15 min. Separately, 0.664 g of KI was dissolved into 20 mL of deionized water under stirring for 30 min, and gradually added to the Bi(NO₃)₃ solution under strong agitation. After the pH was adjusted to 7 with an NH₃ solution, the mixture was transferred to a 100 mL Teflon-lined stainless steel autoclave, and heated at 160 °C for 24 h to obtain C-BiOI powders, which were collected by centrifugation, rinsed with water and ethanol four times, and dried at 60 °C for 18 h. Variable carbon doping was achieved by changing the initial feed of glucose. Four C-BiOI samples were prepared at the C to Bi molar ratios of 1:30, 1:15, 1:6, and 1:2 (denoted as C-BiOI-1, C-BiOI-2, C-BiOI-3, and C-BiOI-4, respectively). From the transient photocurrent responses of the BiOI and C-BiOI samples (Figure 10a), one can see that under simulated sunlight, all C-BiOI photocatalysts show stronger photocurrent responses than pristine BiOI. This is precisely because carbon doping destroyed the periodicity of the crystal lattice and promoted the generation of OVs, which changed the charge distribution in the catalyst and enhanced the IEF, leading to enhanced separation of charge carriers and improved photocatalytic activity.^[150]

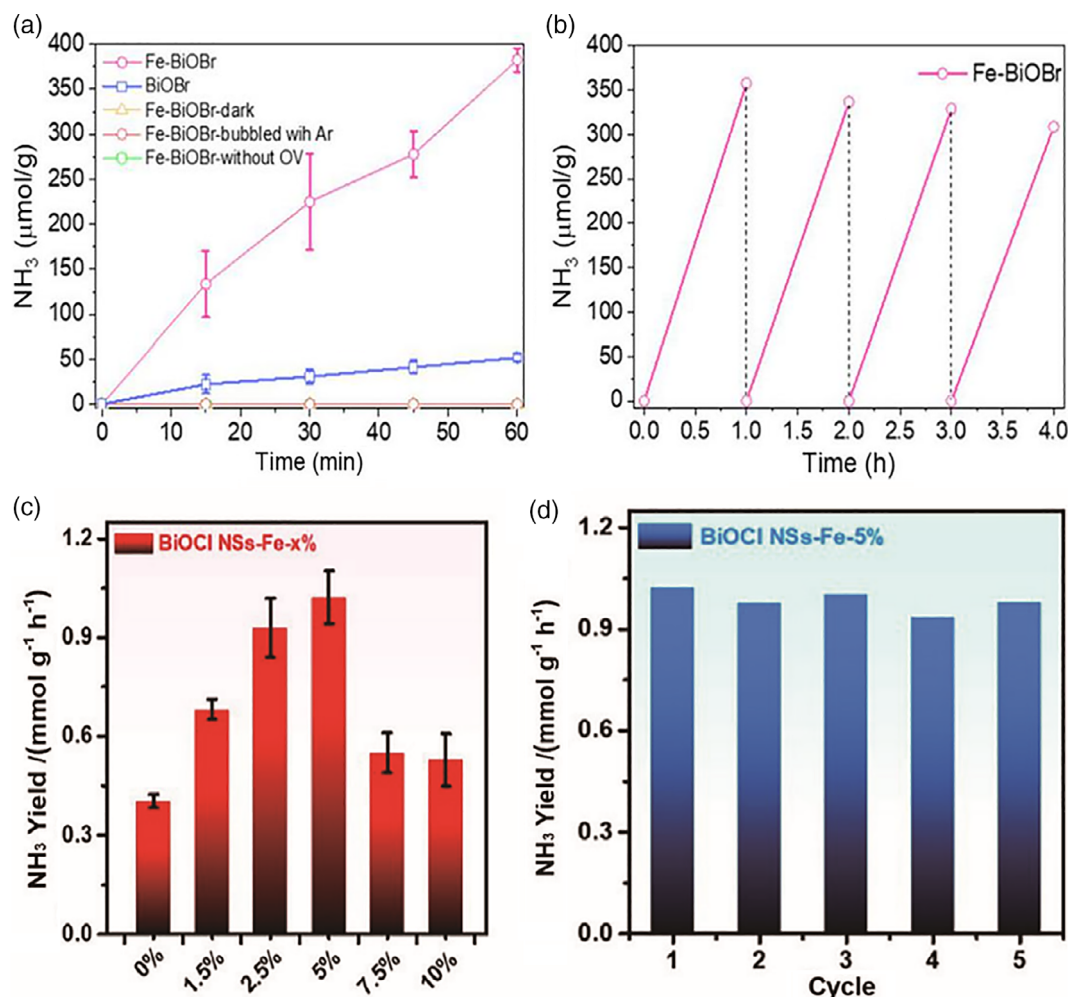


Figure 9. a) Visible light-driven N_2 fixation on Fe-BiOBr and BiOBr, compared with the results of control experiments with Fe-BiOBr in the dark, Ar bubbling, and OV-free Fe-BiOBr. b) Cycling tests of N_2 fixation on Fe-BiOBr. Reproduced with permission.^[106] Copyright 2020, American Chemical Society. c) Photocatalytic NH_3 production rate over the BiOI NSs-Fe-x% in the first 1 h. d) Photocatalytic cycling tests for BiOI NSs-Fe-5%. Reproduced with permission.^[149] Copyright 2019, American Chemical Society.

Interestingly, carbon doping also increased the specific surface area, another contribution to the improved photocatalytic nitrogen fixation performance. From the scanning electron microscopy (SEM) images in Figure 10b and c, C-BiOI can be seen to display a morphology similar to that of BiOI (Figure 10d and e), but the average size of the crystals is smaller, corresponding to a larger specific surface area, which is beneficial to the photocatalytic reaction. This was indeed manifested in photocatalytic nitrogen fixation experiments, where ethanol was used as a hole scavenger and water as the proton source.^[151] From Figure 10f, it can be seen that after carbon was incorporated into the BiOI lattice, the nitrogen fixation rate varied significantly, first increasing and then decreasing with the increase in carbon content. C-BiOI-3 was found to exhibit the highest nitrogen fixation rate at $311 \mu\text{mol L}^{-1} \text{h}^{-1}$, 3.7 times that of pristine BiOI. Furthermore, one can see from Figure 10g that after five test cycles, the photocatalytic performance of C-BiOI-3 only decreased slightly, indicating good stability.

In summary, the fact that the C-doped BiOI samples show significantly improved photocatalytic N_2 fixation, as compared to the pristine counterparts, indicates that elemental doping may be an effective strategy to improve the photocatalytic performance of bismuth oxyhalides toward nitrogen fixation.^[5]

4.2. Heterojunction Composites

The photocatalytic nitrogen fixation performance can also be enhanced by manipulation of the bandgap structure through the formation of heterojunctions, i.e., the formation of composites by combining two semiconductors with different band structures. Figure 11 shows various types of heterostructures produced in bismuth-based photocatalysts reported so far toward N_2 fixation, such as cocatalyst loading, type I heterojunctions, type II heterojunctions, and Z-scheme heterojunctions.^[152–154] The resultant structural changes lead to new properties that are not available in single phase materials. For example, if a

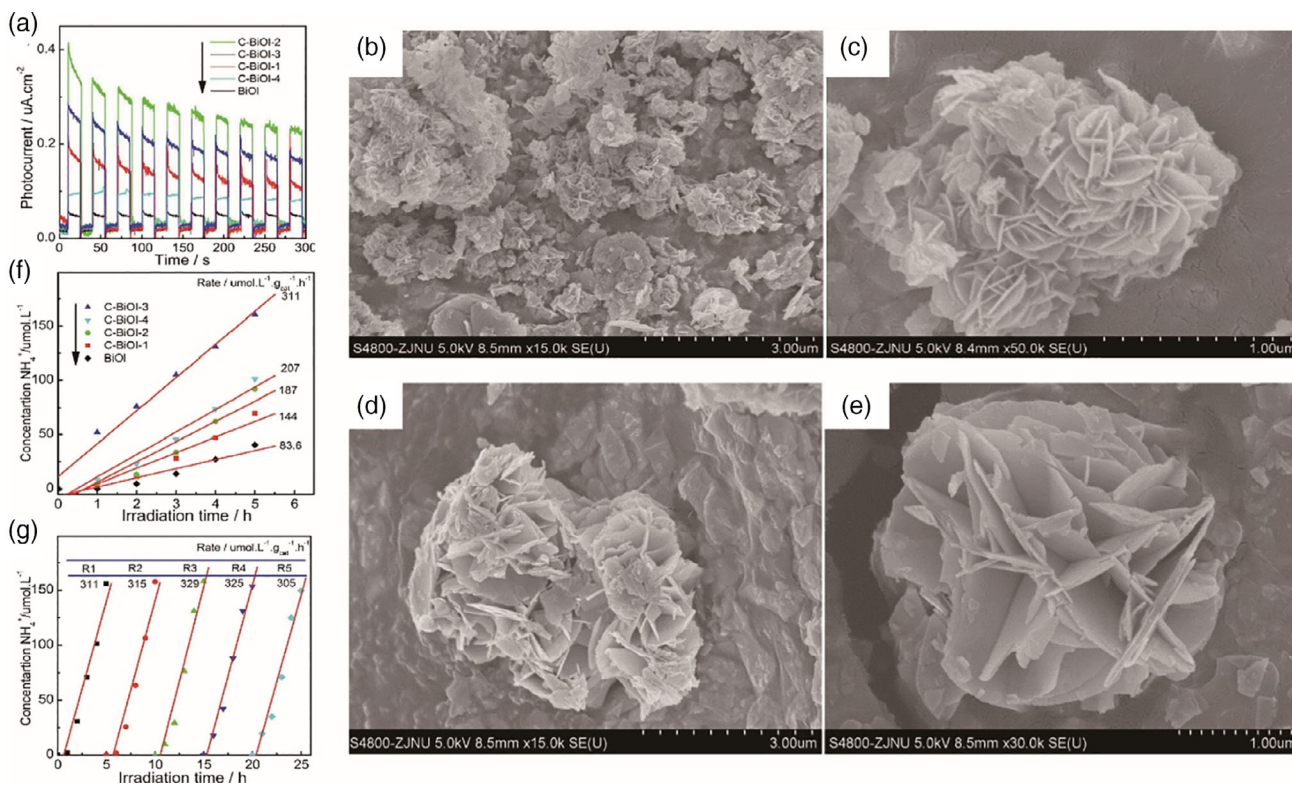


Figure 10. a) Transient photocurrent responses of BiOI and C-BiOI photocatalysts. SEM images of b,c) C-BiOI-2 and d,e) BiOI photocatalysts. f) Photocatalytic N_2 fixation by BiOI and C-BiOI photocatalysts under simulated sunlight. g) Cycling tests of C-BiOI-3. Experimental conditions: 100 mL 5 vol.% ethanol–water solution, with 0.05 g photocatalyst. Reproduced with permission.^[5] Copyright 2018, Elsevier.

wide-bandgap semiconductor is modified by a narrow-bandgap semiconductor, or two kinds of narrow-bandgap semiconductors are combined, the range of photo response of the composite catalysts will be effectively expanded, leading to an enhanced photo energy utilization rate. Therefore, the construction of heterojunctions is effective to boost the performances of a range of photocatalysts.^[24]

Table 3 summarizes recent studies on photocatalytic nitrogen fixation by BiOX catalysts by forming heterojunctions with other materials. For instance, Xiao et al.^[140] successfully constructed

Table 3. Photocatalytic nitrogen fixation of different heterojunction BiOX (X = Cl, Br, and I) materials.

| Heterojunction types | Materials | Nitrogen fixation performance | Ref. |
|-------------------------|--|--|-------|
| Schottky heterojunction | $\text{MoO}_2/\text{BiOCl}$ | $35 \mu\text{mol g}^{-1} \text{h}^{-1}$ | [140] |
| | $\text{H}_{200-1.0} \text{Bi@BiOBr}$ | $181.21 \text{ mol g}^{-1} \text{h}^{-1}$ | [152] |
| | $\text{ZnIn}_2\text{S}_4/2\text{D BiOCl}$ | $14.6 \mu\text{mol g}_{\text{cat}}^{-1} \text{h}^{-1}$ | [67] |
| | $\text{Bi}_4\text{O}_5\text{Br}_2/\text{ZIF-8} (30\%)$ | $327.338 \mu\text{mol L}^{-1} \text{h}^{-1} \text{g}^{-1}$ | [101] |
| Type I heterojunction | $\text{Bi}_2\text{Te}_3/\text{BiOCl}$ | $315.9 \mu\text{mol L}^{-1} \text{h}^{-1}$ | [68] |
| Type II heterojunction | $\text{Bi}_2\text{MoO}_6/\text{OV-BiOBr}$ | $90.7 \mu\text{mol g}^{-1} \text{h}^{-1}$ | [53] |
| | $\text{Bi}_2\text{S}_3/\text{BiOBr}$ | $878 \mu\text{mol g}^{-1}$ | [113] |
| Z-scheme heterojunction | $\text{AgBr}/\text{Bi}_4\text{O}_5\text{Br}_2$ | $179.4 \mu\text{mol L}^{-1} \text{g}^{-1} \text{h}^{-1}$ | [153] |
| | $\beta\text{-Bi}_2\text{O}_3/\text{BiOCl}$ | $102.6 \mu\text{mol L}^{-1}$ | [154] |

$\text{MoO}_2/\text{BiOCl}$ nanocomposites by electrostatic adsorption and observed an excellent photocatalytic nitrogen fixation efficiency when water was used as the proton source. This was due to the strong interactions between BiOCl nanoplates and MoO_2 nanosheets that manipulated the electronic structure of the interface and provided active sites for catalytic reactions. The Mo–O–Bi bond formed at the interface of MoO_2 and BiOCl acted as a bridge for electrons and promoted the separation and migration of photogenerated charge carriers (**Figure 12a**). Also, it can be seen from Figure 12b that in comparison with BiOCl, $\text{MoO}_2/\text{BiOCl}$ showed stronger adsorption of N_2 , which greatly increased the reduction rate of N_2 . Similarly, in $\text{MoO}_2/\text{BiOCl}$, it can be seen that MoO_2 exhibited a nanosheet morphology, and was supported on the surface of BiOCl nanoplates, as evidenced in transmission electron microscopy (TEM) and SEM measurements (Figure 12c–e). From Figure 12f and g, the maximum rate of ammonia production was $\approx 35 \mu\text{mol g}^{-1} \text{h}^{-1}$, eight times higher than that of the original BiOCl and six times higher than that of MoO_2 . Mechanistically, the introduction of MoO_2 enhanced the adsorption and activation of N_2 , due to the formation of Mo–O–Bi bonds at the $\text{MoO}_2/\text{BiOCl}$ interface. Moreover, MoO_2 nanosheets possessed metal-like properties that accelerated electron transfer of BiOCl, and the Mo atoms in MoO_2 can coordinate with N_2 , thereby improving the adsorption and activation of N_2 . Under photoirradiation, the photogenerated holes of BiOCl might transfer to the (110) crystal surface for water oxidation,^[155] and the photogenerated electrons migrated

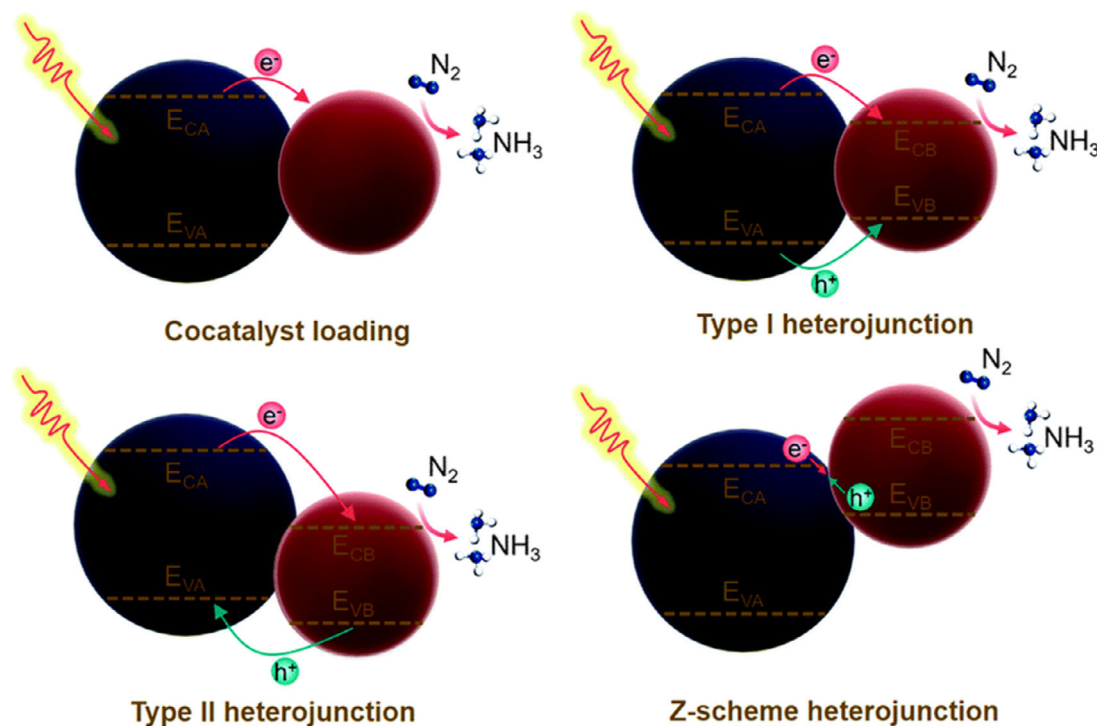


Figure 11. Illustration of different heterostructures for photocatalytic nitrogen reduction to ammonia. Reproduced with permission.^[24] Copyright 2020, Royal Society of Chemistry.

to the interface where MoO_2 and BiOCl were situated for nitrogen fixation reaction (Figure 12a).

In another study, Rong et al.^[68] prepared a type I heterostructure composed of Bi_2Te_3 and BiOCl . From the SEM and TEM images in Figure 13a–d, one can observe that both the pristine BiOCl and $\text{Bi}_2\text{Te}_3/\text{BiOCl}$ composite exhibited a similar flower-like morphology. Yet, the electronic structure and photo response varied markedly, as the CB and VB of the BiOCl sample was identified at -1.1 and $+2.4$ eV, respectively,^[156] whereas those of Bi_2Te_3 at $+0.57$ and $+0.72$ eV, respectively.^[157] From Figure 13e, one can see that because of a small bandgap of only 0.15 eV, Bi_2Te_3 can absorb both UV and visible light, but the low CB (0.57 eV), as compared to that of N_2/NH_3 (-0.092 eV, Figure 2), renders it inactive for N_2 reduction to NH_3 .^[158] For BiOCl , the relatively large bandgap (3.5 eV) indicates that photo absorption is limited to the UV range, whereas the high CB potential (-1.1 eV, Figure 2) is appropriate for N_2 reduction to NH_3 , and the high recombination rate of photogenerated holes and charges in BiOCl limits the photocatalytic activity. For the $\text{Bi}_2\text{Te}_3/\text{BiOCl}$ composite, the photogenerated charge carriers of Bi_2Te_3 effectively suppress the recombination of photogenerated electrons and holes of BiOCl , which prolongs the lifetime of CB electrons in BiOCl and improves the photocatalytic nitrogen fixation performance. From Figure 13f, one can see that under UV radiation, $\text{Bi}_2\text{Te}_3/\text{BiOCl}$ exhibits an effective ammonia release rate of $315.9 \mu\text{mol L}^{-1} \text{h}^{-1}$, much higher than those of BiOCl ($98.2 \mu\text{mol L}^{-1} \text{h}^{-1}$) and $\text{Bi}_2\text{Te}_3/\text{BiOCl}$ ($24.3 \mu\text{mol L}^{-1} \text{h}^{-1}$).

Xue et al.^[53] studied the photocatalytic nitrogen fixation performance of $\text{Bi}_2\text{MoO}_6/\text{OV-BiOBr}$ composites, where type II heterojunctions were formed between n-type Bi_2MoO_6 nanorods

and p-type OV-rich BiOBr nanosheets. MoO_3 nanorods were first prepared by a simple hydrothermal method, and refluxed in a $\text{Bi}(\text{NO}_3)_3$ aqueous solution at 120°C for 4 h to generate Bi_2MoO_6 nanoparticles. Finally, OV- BiOBr nanosheets were grown in situ onto the Bi_2MoO_6 nanosheets by a solvothermal method to produce $\text{Bi}_2\text{MoO}_6/\text{OV-BiOBr}$ composites, which effectively converted N_2 to NH_3 under ambient conditions without using ultrapure water.

From the SEM and TEM images in Figure 14a–c, one can see that the obtained $\text{Bi}_2\text{MoO}_6/\text{OV-BiOBr}$ composite was composed of Bi_2MoO_6 nanorods (about 400–600 nm in diameter) grafted with ultrathin OV- BiOBr nanopetals (10–20 nm in thickness). Electrochemical impedance spectroscopy (EIS) measurements were then conducted to examine the charge-transfer characteristics and interfacial reaction resistance of $\text{Bi}_2\text{MoO}_6/\text{OV-BiOBr}$ composite, Bi_2MoO_6 nanorods, and OV- BiOBr nanosheets both in the dark and under photoirradiation with a 300 W Xe lamp without water absorption. From the Nyquist plots in Figure 14d,e, one can see that in comparison with the original Bi_2MoO_6 nanorods and OV- BiOBr nanosheets, the $\text{Bi}_2\text{MoO}_6/\text{OV-BiOBr}$ composite exhibited a markedly reduced semicircle radius (i.e., charge-transfer resistance, R_{CT}) with and without light illumination, suggesting that the heterostructure can promote interfacial charge transfer. Moreover, the R_{CT} of the $\text{Bi}_2\text{MoO}_6/\text{OV-BiOBr}$ composite was smaller under photoirradiation than that in the dark, likely due to the photo generation of an increasing number of charge carriers. From the UV-vis diffuse reflectance spectroscopy (DRS) measurements (Figure 14f), the absorption threshold (485 nm) of $\text{Bi}_2\text{MoO}_6/\text{OV-BiOBr}$ composite can be seen to be somewhat redshifted,

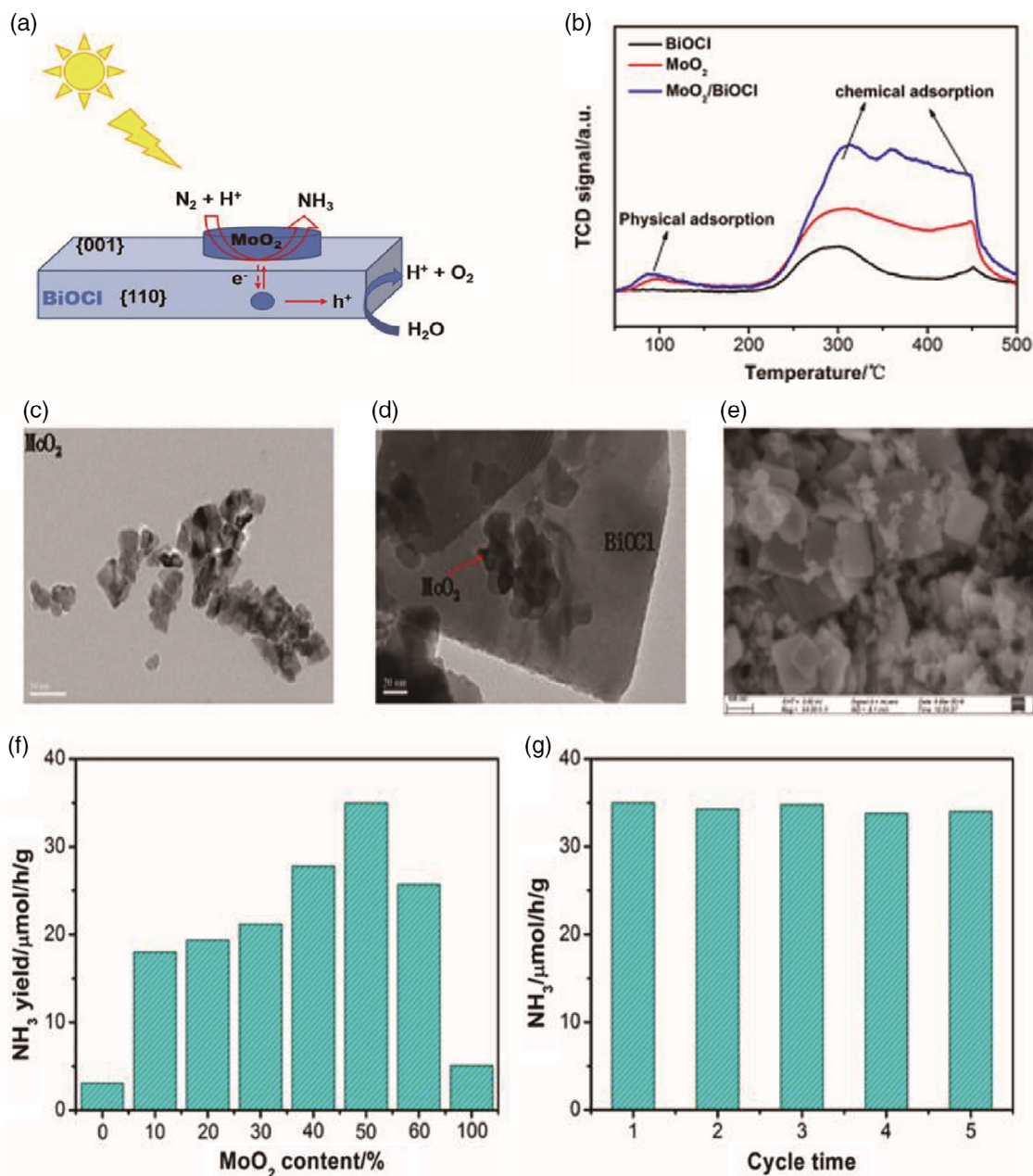


Figure 12. a) Preparation process of $BiOCl/MoO_2$ nanocomposites. b) Nitrogen temperature programmed desorption (N_2 TPD) profiles of the as-prepared $BiOCl$, MoO_2 , and $MoO_2/BiOCl$. TEM images of c) MoO_2 and d) $MoO_2/BiOCl$, e) SEM image of $MoO_2/BiOCl$. f) Photocatalytic N_2 fixation activity of X- $MoO_2/BiOCl$ samples with X equal to 0, 10, 20, 30, 40, 50, 60, 100 (X is the mass fraction) under Xe lamp irradiation. g) Photocatalytic N_2 fixation stability test of X- $MoO_2/BiOCl$ under Xe lamp irradiation. Reproduced with permission.^[140] Copyright 2019, John Wiley & Sons.

in comparison to those of Bi_2MoO_6 (481 nm) and OV- $BiOBr$ (427 nm), suggesting enhanced efficiency of photo energy utilization and therefore the N_2 fixation performance. In addition, from Figure 14g-i, one can see that $Bi_2MoO_6/OV-BiOBr$ exhibits a higher specific surface area than Bi_2MoO_6 nanorods and $BiOBr$ nanosheets, implying enhanced accessibility to the photocatalytic active sites. Moreover, the large number of OVs on the surface of the OV- $BiOBr$ nanosheets is conducive to the adsorption and activation of N_2 molecules.^[158]

Figure 14j and k show the solar-driven N_2 fixation tests of $Bi_2MoO_6/OV-BiOBr$ in pure water and under visible light irradiation (300 W Xe lamp with a 420 nm cutoff filter), which yielded an ammonia production rate of $90.7 \mu mol g^{-1} h^{-1}$ and $81.0 \mu mol g^{-1} h^{-1}$, respectively, far exceeding those by the OV- $BiOBr$ nanosheets ($31.2 \mu mol g^{-1} h^{-1}$) and Bi_2MoO_6 nanocrystals ($3.0 \mu mol g^{-1} h^{-1}$) alone.

Separately, Chen et al.^[153] synthesized $Ag/AgBr/Bi_4O_5Br_2$ nanocomposites by a combination of hydrothermal and ion

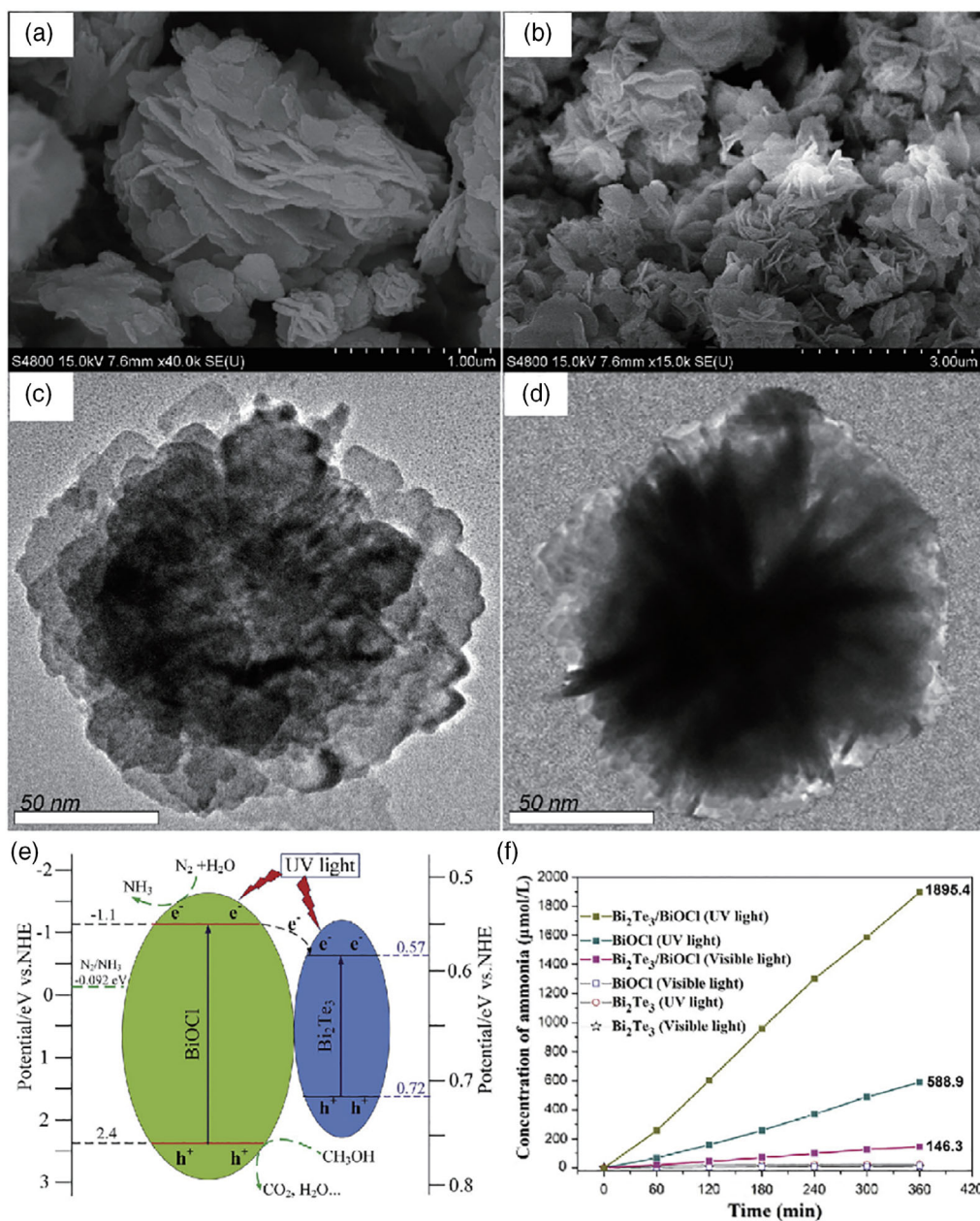


Figure 13. SEM images of a) BiOCl and b) Bi₂Te₃/BiOCl. TEM images of c) BiOCl and d) Bi₂Te₃/BiOCl. e) Schematic illustration of N₂ photofixation over Bi₂Te₃/BiOCl. f) N₂ photofixation activities of photocatalysts. Reproduced with permission.^[68] Copyright 2018, Elsevier.

exchange methods for photocatalytic nitrogen fixation. From the high-resolution TEM image in **Figure 15a**, Bi₄O₅Br₂ can be seen to exhibit well-defined lattice fringes, with an interplanar spacing of 0.278 nm that is consistent with the (020) facets. For the AgBr/Bi₄O₅Br₂ composite (Figure 15b), the lattice fringes of both Bi₄O₅Br₂ and AgBr can be clearly identified. AgBr is a well-known, highly efficient photocatalyst and can effectively prevent the recombination of electron-hole pairs.^[159] Figure 15c shows the transient photocurrent response of AgBr, Bi₄O₅Br₂, and 5.0 wt.% AgBr/Bi₄O₅Br₂ composites under simulated sunlight. All catalysts exhibited a rapid photocurrent response, indicating

facile photogeneration of electrons, and the 5 wt.% AgBr/Bi₄O₅Br₂ sample displayed a maximum photocurrent at about 0.025 μA cm⁻², 2.5 times and 2.8 times higher than those of AgBr and Bi₄O₅Br₂, respectively. Figure 15d shows the EIS curves of the three photocatalysts. The R_{CT} decreases in the order of Bi₄O₅Br₂ > AgBr > 5.0 wt.% AgBr/Bi₄O₅Br₂.^[160] These results show that the loading of AgBr significantly improves the charge-separation efficiency of Bi₄O₅Br₂.^[161] Indeed, it can be seen from Figure 15e that the NH₃ generation rate on AgBr/Bi₄O₅Br₂ under simulated sunlight is much higher than that on pure AgBr or Bi₄O₅Br₂. Among the series of samples,

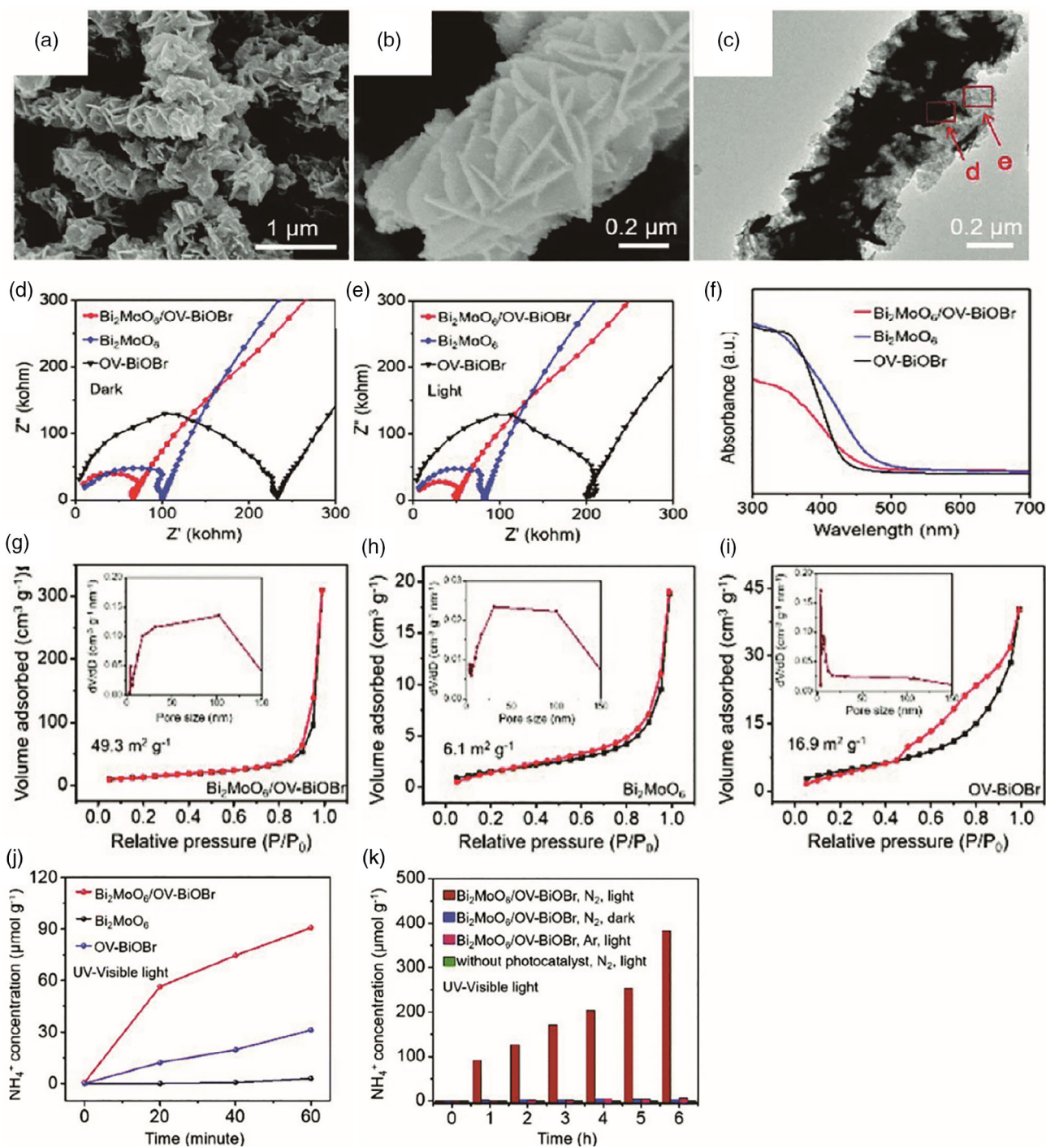


Figure 14. a,b) SEM and c) TEM images of $\text{Bi}_2\text{MoO}_6/\text{OV-BiOBr}$ composites. EIS analysis of $\text{Bi}_2\text{MoO}_6/\text{OV-BiOBr}$ composites, Bi_2MoO_6 nanorods, and OV-BiOBr nanosheets d) in the dark and e) under photoirradiation of a 300 W Xe lamp in ultrapure water. f) UV-vis diffuse reflectance spectra of $\text{Bi}_2\text{MoO}_6/\text{OV-BiOBr}$, Bi_2MoO_6 nanorods, and OV-BiOBr nanosheets. g-i) N_2 adsorption/desorption isotherms and the corresponding pore size distributions of g) $\text{Bi}_2\text{MoO}_6/\text{OV-BiOBr}$ nanocomposites, h) Bi_2MoO_6 nanorods, and i) OV-BiOBr nanosheets. j,k) Solar-driven N_2 fixation tests of $\text{Bi}_2\text{MoO}_6/\text{OV-BiOBr}$, Bi_2MoO_6 nanorods, and OV-BiOBr nanosheets in pure water and under visible light irradiation (300 W Xe lamp with a 420 nm cutoff filter). Reproduced with permission.^[53] Copyright 2019, Royal Society of Chemistry.

the 5.0 wt.% $\text{AgBr}/\text{Bi}_4\text{O}_5\text{Br}_2$ composite showed the best performance, with an NH_3 generation rate of $179.4 \mu\text{mol L}^{-1} \text{g}^{-1} \text{h}^{-1}$, ≈ 3 times those of AgBr ($61.2 \mu\text{mol L}^{-1} \text{g}^{-1} \text{h}^{-1}$) and $\text{Bi}_4\text{O}_5\text{Br}_2$

($56.4 \mu\text{mol L}^{-1} \text{g}^{-1} \text{h}^{-1}$). The cycling tests indicate that the $\text{AgBr}/\text{Bi}_4\text{O}_5\text{Br}_2$ composites also have high photocatalytic stability, with $\approx 90\%$ of the initial rate of NH_3 production retained after

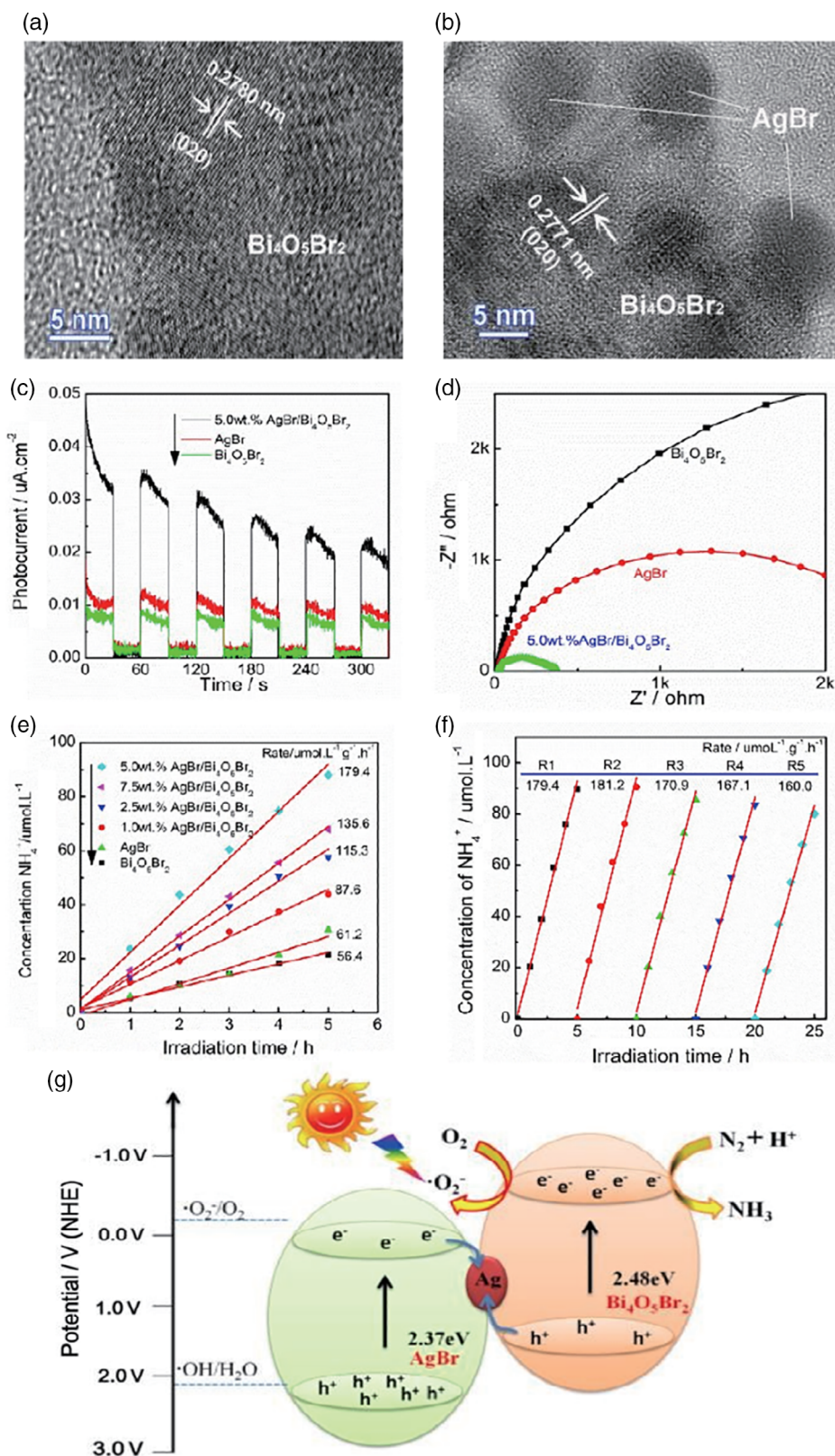


Figure 15. TEM images of a) Bi₄O₅Br₂ and b) AgBr/Bi₄O₅Br₂. c) Photocurrent and d) EIS profiles of Bi₄O₅Br₂, AgBr, and 5.0 wt.% AgBr/Bi₄O₅Br₂ composites. e) Photocatalytic N₂ fixation performance of Bi₄O₅Br₂, AgBr, and AgBr/Bi₄O₅Br₂ composites under simulated sunlight irradiation, and f) the cycling test of 5.0 wt.% AgBr/Bi₄O₅Br₂ composite. g) Possible mechanism of the AgBr/Bi₄O₅Br₂ photocatalyst. Reproduced with permission.^[153] Copyright 2019, Royal Society of Chemistry.

five cycles (Figure 15f). These results indicate that the AgBr/Bi₄O₅Br₂ composite might serve as viable catalysts in photocatalytic N₂ fixation, due to its high photoactivity and stability. This is largely ascribed to the formation of Z-type heterojunctions (Figure 15g), where electrons were accumulated in the Bi₄O₅Br₂ CB, holes remained on the AgBr VB, and Ag nanoparticles likely served as a bridge for charge transfer between the different semiconductors.^[162] The photogenerated electrons of AgBr may migrate to Ag nanoparticles through the Schottky barrier, and react with h⁺ from Bi₄O₅Br₂ VB, thereby effectively promoting the separation of photoinduced electron–hole pairs for photocatalytic reactions.

5. Summary and Perspectives

For a sustainable future, photocatalytic nitrogen reduction provides a promising alternative to the traditional Haber–Bosch process in the production of NH₃. Despite substantial progress in recent years, significant challenges remain in the development of efficient photocatalysts for artificial ammonia production.^[163] Bismuth-based photocatalysts have been proved to be viable for photocatalytic conversion of nitrogen to ammonia, due to the ready formation of OVVs that facilitate the adsorption and activation of N₂, and the performance can be further enhanced by deliberate structural engineering, such as elemental doping and formation of heterojunctions.

It should be recognized that the amount of ammonia produced over the reported photocatalysts has remained small so far. To render the technology feasible for practical applications, significant breakthroughs are needed, by taking advantage of recent progress in the studies of reaction mechanism and catalyst engineering.^[126,156] In particular, as experimental artifacts may interfere with the reliable analysis of photocatalytic nitrogen-to-ammonia conversion,^[24,164] new synthetic and testing protocols are urgently called for. Mechanistically, the introduction of OVVs over bismuth oxyhalides has been known to not only enhance the adsorption and activation of N₂ but also expand the wavelength range of light absorption and electrical conductivity, thereby facilitating the generation and spatial separation of photogenerated electrons and holes. Nonetheless, a complete understanding of the reaction mechanism and pathways of photocatalytic nitrogen fixation remains lacking.^[165] In fact, as multifarious factors can cooperatively contribute to the photocatalytic activity, it is challenging to pinpoint the kinetic bottleneck for photocatalytic nitrogen fixation to ammonia.^[8] In this regard, ingenious design of the photocatalysts with spatially decoupled light absorption unit and surface active sites is highly desired, which would make it possible to deconvolute the contributions of catalytic activity and light absorption to the overall photocatalytic performance of N₂-to-ammonia conversion. Thus, to differentiate the critical contributions of the varied factors to the photoactivity of N₂ fixation to ammonia, rational design of bismuth-based composite photocatalysts with integrated functional components at a system level is crucial to accelerate the progress of nitrogen photoreduction to ammonia.^[134]

In addition, most early studies are focused on improving the conversion efficiency of N₂ to ammonia in the presence of sacrificial agents, and the studies of photocatalysts for the conversion

of N₂ to ammonia and molecular oxygen with pure water have been relatively scarce, which is the ultimate goal of photocatalytic utilization of solar energy and remains a challenge.^[166] For effective reduction of N₂, another key factor that affects the overall photocatalytic reaction efficiency is the oxidation of water to O₂ by photogenerated holes. Considering the slow transfer of photogenerated holes in most photocatalysts to the surface, the multicharge transfer process of water oxidation is a potential rate limiting step. Therefore, for N₂ reduction and water oxidation, deliberate control of the spatial distributions of isolated active centers is likely a viable strategy.^[167]

Acknowledgements

This work was supported by the Natural Science Foundation of China (21471103, 51631001, 21725102, and 21906001), the Scientific Research Base Development Program, and the Science and Technology Innovation Service Ability Construction Project of Beijing Municipal Commission of Education (20530290063). S.W.C. thanks the National Science Foundation for partial support of the work (CHE-2003685). P.S.L. and S.G. contributed equally to this work.

Conflict of Interest

The authors declare no conflict of interest.

Keywords

bismuth oxyhalide, doping, heterostructure, oxygen vacancy, photocatalytic nitrogen fixation

Received: December 14, 2020

Revised: February 28, 2021

Published online:

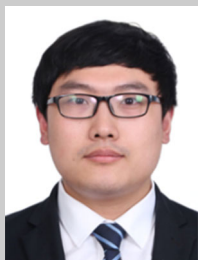
- [1] R. Li, *Chin. J. Catal.* **2018**, *39*, 1180.
- [2] D. Fowler, M. Coyle, U. Skiba, M. A. Sutton, J. N. Cape, S. Reis, L. J. Sheppard, A. Jenkins, B. Grizzetti, J. N. Galloway, P. Vitousek, A. Leach, A. F. Bouwman, K. Butterbach-Bahl, F. Dentener, D. Stevenson, M. Amann, M. Voss, *Philos. Trans. R. Soc. B Biol. Sci.* **2013**, *368*, 20130164.
- [3] A. S. Yasin, B. Liu, N. Wu, T. Musho, *Comput. Mater. Sci.* **2019**, *158*, 65.
- [4] a) X. Rong, H. Chen, J. Rong, X. Zhang, J. Wei, S. Liu, X. Zhou, J. Xu, F. Qiu, Z. Wu, *Chem. Eng. J.* **2019**, *371*, 286; b) W. Liu, K. Yin, K. Yuan, S. Zuo, S. Yang, C. Yao, M. Chen, *Colloids Surf. A* **2020**, *591*, 124488.
- [5] L. Zeng, F. Zhe, Y. Wang, Q. Zhang, X. Zhao, X. Hu, Y. Wu, Y. He, *J. Colloid Interface Sci.* **2019**, *539*, 563.
- [6] X. Gao, Y. Shang, L. Liu, F. Fu, *J. Catal.* **2019**, *371*, 71.
- [7] H. Liu, P. Wu, H. Li, Z. Chen, L. Wang, X. Zeng, Y. Zhu, Y. Jiang, X. Liao, B. S. Haynes, J. Ye, C. Stampfl, J. Huang, *Appl. Catal. B* **2019**, *259*, 118026.
- [8] M. Lan, N. Zheng, X. Dong, C. Hua, H. Ma, X. Zhang, *Dalton Trans.* **2020**, *49*, 9123.
- [9] S. J. Ferguson, *Curr. Opin. Chem. Biol.* **1998**, *2*, 182.
- [10] M. Sevilla, R. H. Burris, N. Gunapala, C. Kennedy, *Mol. Plant Microbe Interact.* **2001**, *14*, 358.

- [11] H. Diarmand-Khalilabad, A. Habibi-Yangjeh, D. Seifzadeh, S. Asadzadeh-Khaneghah, E. Vesali-Kermani, *Ceram. Int.* **2019**, *45*, 2542.
- [12] R. Ding, S. Cao, H. Chen, F. Jiang, X. Wang, *Colloids Surf. A* **2019**, *563*, 263.
- [13] C. Xu, P. Qiu, H. Chen, F. Jiang, *Appl. Surf. Sci.* **2020**, *529*, 147088.
- [14] V. Smil, *Nature* **1999**, *400*, 415.
- [15] C. Liang, H.-Y. Niu, H. Guo, C.-G. Niu, D.-W. Huang, Y.-Y. Yang, H.-Y. Liu, B.-B. Shao, H.-P. Feng, *Chem. Eng. J.* **2020**, *396*, 125395.
- [16] F. Haber, R. Leiser, U.S. Patent 1,269,599, June 18, 1918.
- [17] *Nobel Lectures in Chemistry 1922–1941*, **1999**.
- [18] G. Ertl, *Angew. Chem., Int. Ed.* **2008**, *47*, 3524.
- [19] A. J. Medford, M. C. Hatzell, *ACS Catal.* **2017**, *7*, 2624.
- [20] W. Zhang, Y. Fu, Q. Peng, Q. Yao, X. Wang, A. Yu, Z. Chen, *Chem. Eng. J.* **2020**, *394*, 124822.
- [21] G. Wu, L. Yu, Y. Liu, J. Zhao, Z. Han, G. Geng, *Appl. Surf. Sci.* **2019**, *481*, 649.
- [22] Q. Hao, C. Liu, G. Jia, Y. Wang, H. Arandiyani, W. Wei, B.-J. Ni, *Mater. Horiz.* **2020**, *7*, 1014.
- [23] G. Li, W. Yang, S. Gao, Q. Shen, J. Xue, K. Chen, Q. Li, *Chem. Eng. J.* **2021**, *404*, 127115.
- [24] Y. Huang, N. Zhang, Z. Wu, X. Xie, *J. Mater. Chem. A* **2020**, *8*, 4978.
- [25] N. Cao, G. Zheng, *Nano Res.* **2018**, *11*, 2992.
- [26] K.-Q. Hu, P.-X. Qiu, L.-W. Zeng, S.-X. Hu, L. Mei, S.-W. An, Z.-W. Huang, X.-H. Kong, J.-H. Lan, J.-P. Yu, Z.-H. Zhang, Z.-F. Xu, J. K. Gibson, Z.-F. Chai, Y.-F. Bu, W.-Q. Shi, *Angew. Chem., Int. Ed.* **2020**, *59*, 20666.
- [27] W. Dong, Y. Liu, G. Zeng, T. Cai, L. Shao, H. Chen, W. Zeng, X. Xia, *J. Photochem. Photobiol. A* **2020**, *401*, 112766.
- [28] R. Shi, Y. Zhao, G. I. N. Waterhouse, S. Zhang, T. Zhang, *ACS Catal.* **2019**, *9*, 9739.
- [29] C. Mao, J. Wang, Y. Zou, H. Li, G. Zhan, J. Li, J. Zhao, L. Zhang, *Green Chem.* **2019**, *21*, 2852.
- [30] S. Bian, M. Wen, J. Wang, N. Yang, P. K. Chu, X.-F. Yu, *J. Phys. Chem. Lett.* **2020**, *11*, 1052.
- [31] G. Dong, W. Ho, C. Wang, *J. Mater. Chem. A* **2015**, *3*, 23435.
- [32] Y. Zhang, J. Di, P. Ding, J. Zhao, K. Gu, X. Chen, C. Yan, S. Yin, J. Xia, H. Li, *J. Colloid Interface Sci.* **2019**, *553*, 530.
- [33] Y. Xue, Y. Guo, Z. Liang, H. Cui, J. Tian, *J. Colloid Interface Sci.* **2019**, *556*, 206.
- [34] S. Cao, H. Chen, F. Jiang, X. Wang, *Appl. Catal. B* **2018**, *224*, 222.
- [35] P. Qiu, Z. Liang, X. Liu, X. Qian, H. Cui, J. Tian, *J. Colloid Interface Sci.* **2020**, *571*, 318.
- [36] X. Li, C. He, D. Dai, S. Zuo, X. Yan, C. Yao, C. Ni, *Appl. Nanosci.* **2020**, *10*, 3477.
- [37] a) X. Li, C. He, S. Zuo, X. Yan, D. Dai, Y. Zhang, C. Yao, *Solar Energy* **2019**, *191*, 251; b) H. Wang, Y. Bu, G. Wu, X. Zou, *Dalton Trans.* **2019**, *48*, 11724; c) Z. Wang, X. Hu, Z. Liu, G. Zou, G. Wang, K. Zhang, *ACS Catal.* **2019**, *9*, 10260.
- [38] a) X. Gao, Y. Shang, K. Gao, F. Fu, *Nanomaterials* **2019**, *9*; b) X.-W. Guo, S.-M. Chen, H.-J. Wang, Z.-M. Zhang, H. Lin, L. Song, T.-B. Lu, *J. Mater. Chem. A* **2019**, *7*, 19831; c) X. Gao, Y. Shang, L. Liu, F. Fu, *J. Colloid Interface Sci.* **2019**, *533*, 649; d) J. Wang, W. Lin, Y. Ran, J. Cui, L. Wang, X. Yu, Y. Zhang, *J. Phys. Chem. C* **2020**, *124*, 1253; e) S. Zhou, C. Zhang, J. Liu, J. Liao, Y. Kong, Y. Xu, G. Chen, *Catal. Sci. Technol.* **2019**, *9*, 5562; f) X. Yao, W. Zhang, J. Huang, Z. Du, X. Hong, X. Chen, X. Hu, X. Wang, *Appl. Catal. A* **2020**, *601*, 117647; g) M. Nazemi, M. A. El-Sayed, *Nano Energy* **2019**, *63*, 103886; h) Q. Zheng, Y. Xu, Y. Wan, J. Wu, X. Hu, X. Yao, *J. Nanopart. Res.* **2020**, *22*, 301.
- [39] A. Fujishima, K. Honda, *Nature* **1972**, *238*, 37.
- [40] G. N. Schrauzer, T. D. Guth, *J. Am. Chem. Soc.* **1977**, *22*, 7189.
- [41] G. N. Schrauzer, N. Strampach, L. N. Hui, M. R. Palmer, J. Salehi, *Proc. Natl. Acad. Sci.* **1983**, *80*, 3873.
- [42] a) M. Mohebinia, C. Wu, G. Yang, S. Dai, A. Hakimian, T. Tong, H. Ghasemi, Z. Wang, D. Wang, Z. Ren, J. Bao, *Mater. Today Phys.* **2021**, *16*, 100293; b) C. He, X. Li, X. Chen, S. Ma, X. Yan, Y. Zhang, S. Zuo, C. Yao, *Appl. Clay Sci.* **2020**, *184*, 105398; c) H. Zeng, L. Liu, D. Zhang, Y. Wang, Z. Li, C. Liu, L. Zhang, X. Cui, *Mater. Chem. Phys.* **2021**, *258*, 123830; d) J. Luo, X. Bai, Q. Li, X. Yu, C. Li, Z. Wang, W. Wu, Y. Liang, Z. Zhao, H. Liu, *Nano Energy* **2019**, *66*, 104187; e) X. Zhai, H. Yan, G. Ge, J. Yang, F. Chen, X. Liu, D. Yang, L. Li, J. Zhang, *Appl. Surf. Sci.* **2020**, *506*, 144941; f) M. Ma, X. Han, H. Li, X. Zhang, Z. Zheng, L. Zhou, J. Zheng, Z. Xie, Q. Kuang, L. Zheng, *Appl. Catal. B* **2020**, *265*, 118568; g) X. Feng, H. Chen, F. Jiang, X. Wang, *Catal. Sci. Technol.* **2019**, *9*, 2849; h) R. Tao, X. Li, X. Li, C. Shao, Y. Liu, *Nanoscale* **2020**, *12*, 8320.
- [43] P. Xing, W. Zhang, L. Chen, X. Dai, J. Zhang, L. Zhao, Y. He, *Sustain Energy Fuels* **2020**, *4*, 1112.
- [44] D. Cui, L. Wang, Y. Du, W. Hao, J. Chen, *ACS Sustain Chem. Eng.* **2018**, *6*, 15936.
- [45] A. Harriman, J. M. Thomas, W. Zhou, D. A. Jefferson, *J. Solid State Chem.* **1988**, *72*, 126.
- [46] H. Li, J. Shang, Z. Ai, L. Zhang, *J. Am. Chem. Soc.* **2015**, *137*, 6393.
- [47] H. An, Y. Du, T. Wang, C. Wang, W. Hao, J. Zhang, *Rare Metals* **2008**, *27*, 243.
- [48] L. Ye, Y. Su, X. Jin, H. Xie, C. Zhang, *Environ. Sci. Nano* **2014**, *1*, 90.
- [49] a) Y.-L. Wei, B. Rong, X. Chen, Y.-Y. Ding, Y.-F. Huang, L.-Q. Fan, J.-H. Wu, *Sep. Purif. Technol.* **2021**, *256*, 117815; b) E. Vesali-Kermani, A. Habibi-Yangjeh, S. Ghosh, *Ceram. Int.* **2020**, *46*, 24472; c) H. Wang, R. Zhao, J. Qin, H. Hu, X. Fan, X. Cao, D. Wang, *ACS Appl. Mater. Interfaces* **2019**, *11*, 44249; d) X. Yan, D. Dai, K. Ma, S. Zuo, W. Liu, X. Li, C. Yao, *Front Mater. Sci.* **2020**, *14*, 43; e) R. Guan, D. Wang, Y. Zhang, C. Liu, W. Xu, J. Wang, Z. Zhao, M. Feng, Q. Shang, Z. Sun, *Appl. Catal. B* **2021**, *282*, 119580; f) H. Li, S. Gu, Z. Sun, F. Guo, Y. Xie, B. Tao, X. He, W. Zhang, H. Chang, *J. Mater. Chem. A* **2020**, *8*, 13038; g) H. Zhang, X. Li, H. Su, X. Chen, S. Zuo, X. Yan, W. Liu, C. Yao, *J. Solgel Sci. Technol.* **2019**, *92*, 154.
- [50] a) H. Li, J. Li, Z. Ai, F. Jia, L. Zhang, *Angew. Chem. Int. Ed.* **2018**, *57*, 122; b) J.-X. Yao, D. Bao, Q. Zhang, M.-M. Shi, Y. Wang, R. Gao, J.-M. Yan, Q. Jiang, *Small Methods* **2019**, *3*, 1800333.
- [51] X. Xue, R. Chen, H. Chen, Y. Hu, Q. Ding, Z. Liu, L. Ma, G. Zhu, W. Zhang, Q. Yu, J. Liu, J. Ma, Z. Jin, *Nano Lett* **2018**, *18*, 7372.
- [52] S. Wang, X. Hai, X. Ding, K. Chang, Y. Xiang, X. Meng, Z. Yang, H. Chen, J. Ye, *Adv. Mater.* **2017**, *29*, 1701774.
- [53] X. Xue, R. Chen, C. Yan, Y. Hu, W. Zhang, S. Yang, L. Ma, G. Zhu, Z. Jin, *Nanoscale* **2019**, *11*, 10439.
- [54] C. Liang, H.-Y. Niu, H. Guo, C.-G. Niu, Y.-Y. Yang, H.-Y. Liu, W.-W. Tang, H.-P. Feng, *Chem. Eng. J.* **2021**, *406*, 126868.
- [55] a) L. Yu, Z. Mo, X. Zhu, J. Deng, F. Xu, Y. Song, Y. She, H. Li, H. Xu, *Green Energy Environ.* **2020**, <https://www.sciencedirect.com/science/article/pii/S2468025720300728>; b) S. Liu, Y. Wang, S. Wang, M. You, S. Hong, T.-S. Wu, Y.-L. Soo, Z. Zhao, G. Jiang, Q. Jieshan, B. Wang, Z. Sun, *ACS Sustain. Chem. Eng.* **2019**, *7*, 6813.
- [56] H. Wang, S. Chen, D. Yong, X. Zhang, S. Li, W. Shao, X. Sun, B. Pan, Y. Xie, *J. Am. Chem. Soc.* **2017**, *139*, 4737.
- [57] X. Yang, H. Liu, C. Wang, X. Li, L. Liang, Z. Song, *J. Mater. Sci.: Mater. Electron.* **2020**, *31*, 19647.
- [58] S. Bai, X. Li, Q. Kong, R. Long, C. Wang, J. Jiang, Y. Xiong, *Adv. Mater.* **2015**, *27*, 3444.
- [59] N. R. Dhar, E. V. Seshyacharyulu, S. K. Mukerji, *J. Plant Nutr. Soil Sci.* **1939**, *12*, 222.

- [60] P. Li, Z. Zhou, Q. Wang, M. Guo, S. Chen, J. Low, R. Long, W. Liu, P. Ding, Y. Wu, Y. Xiong, *J. Am. Chem. Soc.* **2020**, *142*, 12430.
- [61] Y.-C. Hao, Y. Guo, L.-W. Chen, M. Shu, X.-Y. Wang, T.-A. Bu, W.-Y. Gao, N. Zhang, X. Su, X. Feng, J.-W. Zhou, B. Wang, C.-W. Hu, A.-X. Yin, R. Si, Y.-W. Zhang, C.-H. Yan, *Nat. Catal.* **2019**, *2*, 448.
- [62] a) T. Fei, L. Yu, Z. Liu, Y. Song, F. Xu, Z. Mo, C. Liu, J. Deng, H. Ji, M. Cheng, Y. Lei, H. Xu, H. Li, *J. Colloid Interface Sci.* **2019**, *557*, 498; b) Z. Ying, S. Chen, S. Zhang, T. Peng, R. Li, *Appl. Catal. B* **2019**, *254*, 351.
- [63] a) M. Barhoumi, M. Said, *Optik* **2020**, *216*, 164631; b) J. Li, Y. Yu, L. Zhang, *Nanoscale* **2014**, *6*, 8473.
- [64] P. Chen, H. Liu, W. Cui, S. C. Lee, L. a. Wang, F. Dong, *EcoMat* **2020**, *2*, e12047.
- [65] K.-L. Zhang, C.-M. Liu, F.-Q. Huang, C. Zheng, W.-D. Wang, *Appl. Catal. B* **2006**, *68*, 125.
- [66] Z.-Y. Zhao, Q.-L. Liu, W.-W. Dai, *Sci. Rep.* **2016**, *6*, 31449.
- [67] L. Guo, X. Han, K. Zhang, Y. Zhang, Q. Zhao, D. Wang, F. Fu, *Catalysts* **2019**, *9*.
- [68] X. Rong, Y. Mao, J. Xu, X. Zhang, L. Zhang, X. Zhou, F. Qiu, Z. Wu, *Catal. Commun.* **2018**, *116*, 16.
- [69] X. Jin, L. Ye, H. Xie, G. Chen, *Coord. Chem. Rev.* **2017**, *349*, 84.
- [70] J. Li, L. Zhang, Y. Li, Y. Yu, *Nanoscale* **2014**, *6*, 167.
- [71] a) X. Lin, T. Huang, F. Huang, W. Wang, J. Shi, *J. Phys. Chem. B* **2006**, *110*, 24629; b) A. K. Chakraborty, M. A. Kebede, *React. Kinet. Mech. Catal.*, **2012**, *106*, 83.
- [72] J. Di, J. Xia, H. Li, S. Guo, S. Dai, *Nano Energy* **2017**, *41*, 172.
- [73] J. Li, H. Li, G. Zhan, L. Zhang, *Acc. Chem. Res.* **2017**, *50*, 112.
- [74] Z. Wang, M. Chen, D. Huang, G. Zeng, P. Xu, C. Zhou, C. Lai, H. Wang, M. Cheng, W. Wang, *Chem. Eng. J.* **2019**, *374*, 1025.
- [75] a) R. a. He, S. Cao, P. Zhou, J. Yu, *Chin. J. Catal.* **2014**, *35*, 989; b) K. Xu, L. Wang, X. Xu, S. X. Dou, W. Hao, Y. Du, *Energy Storage Mater.* **2019**, *19*, 446.
- [76] X. Chang, M. A. Gondal, A. A. Al-Saadi, M. A. Ali, H. Shen, Q. Zhou, J. Zhang, M. Du, Y. Liu, G. Ji, *J. Colloid Interface Sci.* **2012**, *377*, 291.
- [77] K. Ren, J. Liu, J. Liang, K. Zhang, X. Zheng, H. Luo, Y. Huang, P. Liu, X. Yu, *Dalton Trans.* **2013**, *42*, 9706.
- [78] Y. Li, J. Wang, H. Yao, L. Dang, Z. Li, *J. Mol. Catal. A Chem.* **2011**, *334*, 116.
- [79] X. Wu, C. Y. Toe, C. Su, Y. H. Ng, R. Amal, J. Scott, *J. Mater. Chem. A* **2020**, *8*, 15302.
- [80] Z. Jiang, F. Yang, G. Yang, L. Kong, M. O. Jones, T. Xiao, P. P. Edwards, *J. Photochem. Photobiol. A* **2010**, *212*, 8.
- [81] S. Peng, L. Li, P. Zhu, Y. Wu, M. Srinivasan, S. G. Mhaisalkar, S. Ramakrishna, Q. Yan, *Chem. Asian J.* **2013**, *8*, 258.
- [82] J.-M. Song, C.-J. Mao, H.-L. Niu, Y.-H. Shen, S.-Y. Zhang, *CrystEngComm* **2010**, *12*, 3875.
- [83] J. Xiong, G. Cheng, G. Li, F. Qin, R. Chen, *RSC Adv* **2011**, *1*, 1542.
- [84] J. Xu, W. Meng, Y. Zhang, L. Li, C. Guo, *Appl. Catal. B* **2011**, *107*, 355.
- [85] Y. Feng, L. Li, J. Li, J. Wang, L. Liu, *J. Hazard Mater.* **2011**, *192*, 538.
- [86] W. L. Huang, Q. Zhu, *Comput. Mater. Sci.* **2008**, *43*, 1101.
- [87] X. Chang, J. Huang, C. Cheng, Q. Sui, W. Sha, G. Ji, S. Deng, G. Yu, *Catal. Commun.* **2010**, *11*, 460.
- [88] J. Henle, P. Simon, A. Frenzel, S. Scholz, S. Kaskel, *Chem. Mater.* **2007**, *19*, 366.
- [89] L. Ye, L. Zan, L. Tian, T. Peng, J. Zhang, *Chem. Commun.* **2011**, *47*, 6951.
- [90] C. Wang, X. Zhang, B. Yuan, C. Shao, Y. Liu, *Micro Nano Lett.* **2012**, *7*, 152.
- [91] H. Cheng, B. Huang, Z. Wang, X. Qin, X. Zhang, Y. Dai, *Chem. Eur. J.* **2011**, *17*, 8039.
- [92] L. Zhang, X.-F. Cao, X.-T. Chen, Z.-L. Xue, *J. Colloid Interface Sci.* **2011**, *354*, 630.
- [93] I. K. Konstantinou, T. A. Albanis, *Appl. Catal. B* **2004**, *49*, 1.
- [94] J. Xia, S. Yin, H. Li, H. Xu, Y. Yan, Q. Zhang, *Langmuir* **2011**, *27*, 1200.
- [95] L. Ye, L. Tian, T. Peng, L. Zan, *J. Mater. Chem.* **2011**, *21*, 12479.
- [96] H. Chen, C. E. Nanayakkara, V. H. Grassian, *Chem. Rev.* **2012**, *112*, 5919.
- [97] C. Ding, L. Ye, Q. Zhao, Z. Zhong, K. Liu, H. Xie, K. Bao, X. Zhang, Z. Huang, *J. CO2 Util.* **2016**, *14*, 135.
- [98] Y. Bai, L. Ye, T. Chen, L. Wang, X. Shi, X. Zhang, D. Chen, *ACS Appl. Mater. Interfaces* **2016**, *8*, 27661.
- [99] Y. Bi, Y. Wang, X. Dong, N. Zheng, H. Ma, X. Zhang, *RSC Adv.* **2018**, *8*, 21871.
- [100] J. Di, J. Xia, M. F. Chisholm, J. Zhong, C. Chen, X. Cao, F. Dong, Z. Chi, H. Chen, Y.-X. Weng, J. Xiong, S.-Z. Yang, H. Li, Z. Liu, S. Dai, *Adv. Mater.* **2019**, *31*, 1807576.
- [101] J. Liu, R. Li, X. Zu, X. Zhang, Y. Wang, Y. Wang, C. Fan, *Chem. Eng. J.* **2019**, *371*, 796.
- [102] H. Li, J. Shang, J. Shi, K. Zhao, L. Zhang, *Nanoscale* **2016**, *8*, 1986.
- [103] D. Wu, R. Wang, C. Yang, Y. An, H. Lu, H. Wang, K. Cao, Z. Gao, W. Zhang, F. Xu, K. Jiang, *J. Colloid Interface Sci.* **2019**, *556*, 111.
- [104] S. Chen, D. Liu, T. Peng, *Solar RRL* **2021**, *5*, 2000487.
- [105] a) X. Li, J. Xiong, X. Gao, J. Ma, Z. Chen, B. Kang, J. Liu, H. Li, Z. Feng, J. Huang, *J. Hazard Mater.* **2020**, *387*, 121690; b) W. Gu, X. Li, W. Zhang, J. Wang, X. Yin, L. Zhu, Z. Chen, W. Zou, Z. Fu, Y. Lu, *Appl. Surf. Sci.* **2019**, *479*, 137; c) W. Wu, Z. Zhang, J. Di, W. Zhao, *ChemNanoMat* **2019**, *5*, 215; d) M. Lv, S. Jin, H. Wang, Y. Chen, T. Ma, K. Cui, J. Li, S. Wu, Z. Liu, Y. Guo, Z. Liu, X. Chang, X. Li, *Catal. Sci. Technol.* **2020**, *10*, 4786; e) L. Bai, F. Ye, L. Li, J. Lu, S. Zhong, S. Bai, *Small* **2017**, *13*, 1701607.
- [106] Y. Liu, Z. Hu, J. C. Yu, *Chem. Mater.* **2020**, *32*, 1488.
- [107] a) J. Wang, Y. Wei, B. Yang, B. Wang, J. Chen, H. Jing, *J. Catal.* **2019**, *377*, 209; b) D. Wu, L. Ye, H. Y. Yip, P. K. Wong, *Catal. Sci. Technol.* **2017**, *7*, 265.
- [108] a) J. Jin, Y. Wang, T. He, *RSC Adv.* **2015**, *5*, 100244; b) L. Tang, R. Chen, X. Meng, B. Lv, F. Fan, J. Ye, X. Wang, Y. Zhou, C. Li, Z. Zou, *Chem. Commun.* **2018**, *54*, 5126.
- [109] a) X. Xiao, Y. Lin, B. Pan, W. Fan, Y. Huang, *Inorg. Chem. Commun.* **2018**, *93*, 65; b) X. Liu, L. Cai, *Appl. Surf. Sci.* **2018**, *445*, 242; c) L. Ye, J. Liu, Z. Jiang, T. Peng, L. Zan, *Appl. Catal. B* **2013**, *142–143*, 1; d) G. Xu, M. Li, Y. Wang, N. Zheng, L. Yang, H. Yu, Y. Yu, *Sci. Total Environ.* **2019**, *678*, 173; e) A. M. Alansi, M. Al-Qunaibit, I. O. Alade, T. F. Qahtan, T. A. Saleh, *J. Mol. Liq.* **2018**, *253*, 297.
- [110] a) S. Hu, X. Chen, Q. Li, Y. Zhao, W. Mao, *Catal. Sci. Technol.* **2016**, *6*, 5884; b) Q. Zhang, S. Hu, Z. Fan, D. Liu, Y. Zhao, H. Ma, F. Li, *Dalton Trans.* **2016**, *45*, 3497.
- [111] X. Gao, Y. Wen, D. Qu, L. An, S. Luan, W. Jiang, X. Zong, X. Liu, Z. Sun, *ACS Sustain Chem. Eng.* **2018**, *6*, 5342.
- [112] Y. Zhao, R. Shi, X. Bian, C. Zhou, Y. Zhao, S. Zhang, F. Wu, G. I. N. Waterhouse, L.-Z. Wu, C.-H. Tung, T. Zhang, *Adv. Sci.* **2019**, *6*, 1802109.
- [113] F. Xu, C. Xu, D. Wu, Z. Gao, X. Ma, K. Jiang, *Mater. Lett.* **2019**, *253*, 183.
- [114] X. Wu, K. Zhang, G. Zhang, S. Yin, *Chem. Eng. J.* **2017**, *325*, 59.
- [115] J. G. Chen, R. M. Crooks, L. C. Seefeldt, K. L. Bren, R. M. Bullock, M. Y. Darensbourg, P. L. Holland, B. Hoffman, M. J. Janik, A. K. Jones, M. G. Kanatzidis, P. King, K. M. Lancaster, S. V. Lymar, P. Pfromm, W. F. Schneider, R. R. Schrock, *Science* **2018**, *360*, eaar6611.
- [116] G. Wu, Y. Gao, B. Zheng, *Ceram. Int.* **2016**, *42*, 6985.
- [117] a) S. Sun, Q. An, W. Wang, L. Zhang, J. Liu, W. A. Goddard Iii, *J. Mater. Chem. A* **2017**, *5*, 201; b) K. C. MacLeod, D. J. Vinyard, P. L. Holland, *J. Am. Chem. Soc.* **2014**, *136*, 10226; c) G. Gu,

- K. Wang, N. Xiong, Z. Li, Z. Fan, S. Hu, X. Zou, *Dalton Trans.* **2019**, 48, 5083.
- [118] a) J. Ding, Q. Zhong, H. Gu, *J. Alloys Compd.* **2018**, 746, 147; b) K. Bhattacharyya, A. Datta, *Phys. Chem. Chem. Phys.* **2019**, 21, 12346.
- [119] S. Sultana, S. Mansingh, K. M. Parida, *J. Mater. Chem. A* **2019**, 7, 9145.
- [120] M. Elitzur, *Science* **2005**, 309, 71.
- [121] F. Chen, H. Huang, L. Ye, T. Zhang, Y. Zhang, X. Han, T. Ma, *Adv. Funct. Mater.* **2018**, 28, 1804284.
- [122] L. Ye, X. Jin, Y. Leng, Y. Su, H. Xie, C. Liu, *J. Power Sources* **2015**, 293, 409.
- [123] Y. Hao, X. Dong, S. Zhai, H. Ma, X. Wang, X. Zhang, *Chem. Eur. J.* **2016**, 22, 18722.
- [124] A. L. Linsebigler, G. Lu, J. T. Yates, *Chem. Rev.* **1995**, 95, 735.
- [125] A. Kudo, Y. Miseki, *Chem. Soc. Rev.* **2009**, 38, 253.
- [126] a) W. Ren, Z. Mei, S. Zheng, S. Li, Y. Zhu, J. Zheng, Y. Lin, H. Chen, M. Gu, F. Pan, *Research* **2020**, 2020, 3750314; b) Z. Li, Z. Gao, B. Li, L. Zhang, R. Fu, Y. Li, X. Mu, L. Li, *Appl. Catal. B* **2020**, 262, 118276; c) J. Yang, *J. Chem* **2018**, 2018, 3286782; d) L. Shi, Z. Li, L. Lu, A. Carrasco-Pena, N. Orlovskaya, H. Zhou, Y. Yang, *J. Mater. Chem. A* **2020**, 8, 1059; e) M. Zheng, Y. Li, K. Ding, Y. Zhang, W. Chen, W. Lin, *Phys. Chem. Chem. Phys.* **2020**, 22, 21872.
- [127] a) A. Shi, H. Li, S. Yin, Z. Hou, J. Rong, J. Zhang, Y. Wang, *Appl. Catal. B* **2018**, 235, 197; b) T.-A. Bu, Y.-C. Hao, W.-Y. Gao, X. Su, L.-W. Chen, N. Zhang, A.-X. Yin, *Nanoscale* **2019**, 11, 10072; c) X. Feng, H. Chen, F. Jiang, X. Wang, *J. Colloid Interface Sci.* **2018**, 509, 298; d) E. Mateo-Marti, S. Galvez-Martinez, C. Gil-Lozano, M.-P. Zorzano, *Sci. Rep.* **2019**, 9, 15311.
- [128] a) Z. Ding, S. Wang, X. Chang, D.-H. Wang, T. Zhang, *RSC Adv.* **2020**, 10, 26246; b) S. Chang, X. Xu, *Inorg. Chem. Front.* **2020**, 7, 620; c) A. Pandikumar, S. Manonmani, R. Ramaraj, *Catal. Sci. Technol.* **2012**, 2, 345.
- [129] a) Y. Zhao, L. Zheng, R. Shi, S. Zhang, X. Bian, F. Wu, X. Cao, G. I. N. Waterhouse, T. Zhang, *Adv. Energy Mater.* **2020**, 10, 2002199; b) B. Liu, J. Qin, H. Yang, X. Hu, W. Zhao, Z. Zhang, *ChemCatChem* **2020**, 12, 5221; c) H. Jiang, C. Zang, Y. Zhang, W. Wang, C. Yang, B. Sun, Y. Shen, F. Bian, *Catal. Sci. Technol.* **2020**, 10, 5964.
- [130] S. Mansingh, K. K. Das, A. Behera, S. Subudhi, S. Sultana, K. Parida, *Nanoscale Adv.* **2020**, 2, 2004.
- [131] T. Hou, Q. Li, Y. Zhang, W. Zhu, K. Yu, S. Wang, Q. Xu, S. Liang, L. Wang, *Appl. Catal. B* **2020**, 273, 119072.
- [132] a) Q. Wu, R. van de Krol, *J. Am. Chem. Soc.* **2012**, 134, 9369; b) M. Long, L. Zheng, *Chin. J. Catal.* **2017**, 38, 617; c) M. Guan, C. Xiao, J. Zhang, S. Fan, R. An, Q. Cheng, J. Xie, M. Zhou, B. Ye, Y. Xie, *J. Am. Chem. Soc.* **2013**, 135, 10411.
- [133] X. Pan, M.-Q. Yang, X. Fu, N. Zhang, Y.-J. Xu, *Nanoscale* **2013**, 5.
- [134] C. J. M. van der Ham, M. T. M. Koper, D. G. H. Hetterscheid, *Chem. Soc. Rev.* **2014**, 43, 5183.
- [135] a) F. Chen, Z. Ma, L. Ye, T. Ma, T. Zhang, Y. Zhang, H. Huang, *Adv. Mater.* **2020**, 32, 1908350; b) Y. Hao, X. Dong, X. Wang, H. Ma, X. Zhang, *J. Mater. Chem. A* **2017**, 5, 5426; c) N. Zhang, A. Jalil, D. Wu, S. Chen, Y. Liu, C. Gao, W. Ye, Z. Qi, H. Ju, C. Wang, X. Wu, L. Song, J. Zhu, Y. Xiong, *J. Am. Chem. Soc.* **2018**, 140, 9434.
- [136] H. Tan, Z. Zhao, W.-b. Zhu, E. N. Coker, B. Li, M. Zheng, W. Yu, H. Fan, Z. Sun, *ACS Appl. Mater. Interfaces* **2014**, 6, 19184.
- [137] J. John, D.-K. Lee, U. Sim, *Nano Convergence* **2019**, 6, 15.
- [138] T. Hou, Y. Xiao, P. Cui, Y. Huang, X. Tan, X. Zheng, Y. Zou, C. Liu, W. Zhu, S. Liang, L. Wang, *Adv. Energy Mater.* **2019**, 9, 1902319.
- [139] a) L. Zhang, W. Wang, D. Jiang, E. Gao, S. Sun, *Nano Res.* **2015**, 8, 821; b) C. Guo, J. Ran, A. Vasileff, S.-Z. Qiao, *Energy Environ. Sci.* **2018**, 11, 45.
- [140] C. Xiao, H. Wang, L. Zhang, S. Sun, W. Wang, *ChemCatChem* **2019**, 11, 6467.
- [141] S. Hu, X. Chen, Q. Li, F. Li, Z. Fan, H. Wang, Y. Wang, B. Zheng, G. Wu, *Appl. Catal. B* **2017**, 201, 58.
- [142] Y.-H. Liu, M. H. Vu, J. Lim, T.-O. Do, M. C. Hatzell, *Faraday Discuss.* **2019**, 215, 379.
- [143] D. Jayasri, S. S. Narayanan, *J. Hazard. Mater.* **2007**, 144, 348.
- [144] W. Li, X. Geng, F. Xiao, G. An, D. Wang, *ChemCatChem* **2017**, 9, 3762.
- [145] a) H. Li, J. Shi, K. Zhao, L. Zhang, *Nanoscale* **2014**, 6, 14168; b) X. Wang, C. Zhou, L. Yin, R. Zhang, G. Liu, *ACS Sustainable Chem. Eng.* **2019**, 7, 7900.
- [146] X. Ding, K. Zhao, L. Zhang, *Environ. Sci. Technol.* **2014**, 48, 5823.
- [147] Z. Liu, B. Wu, Y. Zhu, D. Yin, L. Wang, *Catal. Lett.* **2012**, 142, 1489.
- [148] H. Hirakawa, M. Hashimoto, Y. Shiraishi, T. Hirai, *J. Am. Chem. Soc.* **2017**, 139, 10929.
- [149] N. Zhang, L. Li, Q. Shao, T. Zhu, X. Huang, X. Xiao, *ACS Appl. Energy Mater.* **2019**, 2, 8394.
- [150] a) J. Li, K. Zhao, Y. Yu, L. Zhang, *Adv. Funct. Mater.* **2015**, 25, 2189; b) S. Liu, C. Li, J. Yu, Q. Xiang, *CrystEngComm* **2011**, 13, 2533; c) K. Wang, G. Gu, S. Hu, J. Zhang, X. Sun, F. Wang, P. Li, Y. Zhao, Z. Fan, X. Zou, *Chem. Eng. J.* **2019**, 368, 896; d) S.-X. Wang, H. Maimaiti, B. Xu, Y. Guo, P.-s. Zhai, H.-z. Zhang, *J. Phys. Chem. A* **2019**, 123, 31119.
- [151] T. Oshikiri, K. Ueno, H. Misawa, *Angew. Chem. Int. Ed.* **2016**, 55, 3942.
- [152] C. Hua, X. Dong, Y. Wang, N. Zheng, H. Ma, X. Zhang, *J. Mater. Sci.* **2019**, 54, 9397.
- [153] Y. Chen, C. Zhao, S. Ma, P. Xing, X. Hu, Y. Wu, Y. He, *Inorg. Chem. Front.* **2019**, 6, 3083.
- [154] J. Shang, H. Chen, B. Zhao, F. Zhou, H. Zhang, X. Wang, *J. Mater. Sci.* **2019**, 30, 17956.
- [155] L. Zhang, Z. Han, W. Wang, X. Li, Y. Su, D. Jiang, X. Lei, S. Sun, *Chem. Eur. J.* **2015**, 21, 18089.
- [156] S. Y. Chai, Y. J. Kim, M. H. Jung, A. K. Chakraborty, D. Jung, W. I. Lee, *J. Catal.* **2009**, 262, 144.
- [157] H. Li, J. Liu, W. Hou, N. Du, R. Zhang, X. Tao, *Appl. Catal. B* **2014**, 160–161, 89.
- [158] C. Xiao, H. Hu, X. Zhang, D. R. MacFarlane, *ACS Sustain. Chem. Eng.* **2017**, 5, 10858.
- [159] a) T. Li, Y. He, H. Lin, J. Cai, L. Dong, X. Wang, M. Luo, L. Zhao, X. Yi, W. Weng, *Appl. Catal. B* **2013**, 138–139, 95; b) J. Cao, B. Luo, H. Lin, S. Chen, *J. Mol. Catal. A Chem.* **2011**, 344, 138; c) Z. Wang, J. Zhang, J. Lv, K. Dai, C. Liang, *Appl. Surf. Sci.* **2017**, 396, 791; d) X. Zhang, C. Wang, C. Yu, B. Teng, Y. He, L. Zhao, M. Fan, *J. Environ. Sci.* **2018**, 63, 68; e) M. Ge, W. Liu, X.-R. Hu, Z.-L. Li, *J. Phys. Chem. Solids* **2017**, 109, 1; f) L. Kong, Z. Jiang, H. H. Lai, R. J. Nicholls, T. Xiao, M. O. Jones, P. P. Edwards, *J. Catal.* **2012**, 293, 116; g) Y. Zhou, J. Li, C. Liu, P. Huo, H. Wang, *Appl. Surf. Sci.* **2018**, 458, 586; h) J. Xiong, W. Li, Y. Gan, Y. Wei, G. Cheng, S. Dou, Z. Li, *Inorg. Chem. Front.* **2018**, 5, 2432.
- [160] a) J. Yu, Z. Chen, Q. Chen, Y. Wang, H. Lin, X. Hu, L. Zhao, Y. He, *Int. J. Hydrogen Energy* **2018**, 43, 4347; b) P. Xing, Z. Chen, P. Chen, H. Lin, L. Zhao, Y. Wu, Y. He, *J. Colloid Interface Sci.* **2019**, 552, 622; c) B. Li, R. Wang, X. Shao, L. Shao, B. Zhang, *Inorg. Chem. Front.* **2017**, 4, 2088.
- [161] a) J. Yu, Z. Chen, L. Zeng, Y. Ma, Z. Feng, Y. Wu, H. Lin, L. Zhao, Y. He, *Sol Energy Mater. Sol. Cells* **2018**, 179, 45; b) P. Chen, P. Xing, Z. Chen, X. Hu, H. Lin, L. Zhao, Y. He, *J. Colloid Interface Sci.* **2019**, 534, 163.
- [162] a) S. Ding, M. Han, Y. Dai, S. Yang, D. Mao, H. He, C. Sun, *ChemCatChem* **2019**, 11, 3490; b) X.-J. Wen, C.-G. Niu, L. Zhang,

- C. Liang, H. Guo, G.-M. Zeng, *J. Catal.* **2018**, 358, 141; c) H. Guo, C.-G. Niu, X.-J. Wen, L. Zhang, C. Liang, X.-G. Zhang, D.-L. Guan, N. Tang, G.-M. Zeng, *J. Colloid Interface Sci.* **2018**, 513, 852.
 [163] R. Li, *Chin. J. Catal.* **2017**, 38, 5.
 [164] K. Li, D. Martin, J. Tang, *Chin. J. Catal.* **2011**, 32, 879.
 [165] X. Xue, R. Chen, C. Yan, P. Zhao, Y. Hu, W. Zhang, S. Yang, Z. Jin, *Nano Res.* **2019**, 12, 1229.
 [166] T. H. Rod, A. Logadottir, J. K. Nørskov, *J. Chem. Phys.* **2000**, 112, 5343.
 [167] a) E. Skúlason, T. Bligaard, S. Gudmundsdóttir, F. Studt, J. Rossmeisl, F. Abild-Pedersen, T. Vegge, H. Jónsson, J. K. Nørskov, *Phys. Chem. Chem. Phys.* **2012**, 14, 1235; b) Y. Abghoui, A. L. Garden, J. G. Howalt, T. Vegge, E. Skúlason, *ACS Catal.* **2016**, 6, 635.



Peishen Li received his master's degree in engineering from the Capital Normal University in June 2020, under joint supervision by Professor Qiang Wang, College of Elementary Education, Capital Normal University, and Professor. Wen Liu, School of Environmental Science and Engineering, Peking University. After graduation, he works as a research assistant in Professor Liu's group. His research interests include the degradation of pollutants in water and photocatalytic nitrogen fixation and NH_3 catalytic reduction of NO_x .



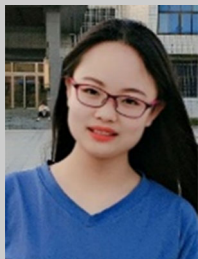
Shuai Gao is pursuing a master's degree in engineering from the Capital Normal University under the guidance of Professor Qiang Wang. His current research interests focus on photocatalytic N_2 fixation over bismuth-based catalysts.



Qiming Liu received his B.E. degree in material chemistry in 2018 from the Central South University, Hunan, China, and joined Professor Shaowei Chen's lab at the University of California Santa Cruz to pursue a Ph.D. degree. His research interests concentrate on single-atom electrocatalysts, surface functionalization of nanoparticles for electrochemical energy conversion and storage, and density functional theory.



Peiren Ding is pursuing a master's degree in engineering from the Capital Normal University under the guidance of Professor Qiang Wang. His research interests are photocatalytic degradation of organic pollutants in environmental waters and photocatalytic nitrogen fixation.



Yunyun Wu is pursuing a master's degree in the Capital Normal University under the supervision of Professor Qiang Wang. Her research interest is focused on micro-sized functional materials and photocatalytic degradation of organic pollutants in environmental waters.



Changzheng Wang received his M.S. degree (2005) from the Yunnan Normal University and Ph.D. (2008) from Beijing Normal University. Currently, he is a professor in the School of Environment and Engineering, Beijing University of Civil Engineering and Architecture. His research focuses on the synthesis of functional nanomaterials for environmental remediation and their applications in photocatalyst and electrocatalyst.



Shaobin Yu is pursuing a master's degree in engineering from the Beijing University of Civil Engineering and Architecture under the guidance of Professor Changzheng Wang. His research interest is focused on titanium dioxide photocatalytic degradation of antibiotic drugs in water.



Wen Liu is a professor in the College of Environmental Sciences and Engineering at Peking University, China. He is also the associate director of the Department of Environmental Engineering, and the head of Environmental Nanotechnology Lab in the Peking University. He received his B.S. degree from the Nankai University in 2009 and Ph.D. from Peking University in 2014. His research interests include environmental nanotechnology, functional materials synthesis and application, water and wastewater treatment, etc.



Qiang Wang received his M.S. degree (2004) from the Yunnan Normal University, Ph.D. (2007) from Beijing Institute of Technology, and was a visiting scholar in Benjamin J. Wiley's lab at the Duke University (2011–2012). He founded the Laboratory for Micro-Sized Functional Materials in Capital Normal University. Now, he is a professor in the College of Elementary Education of Capital Normal University. His research focuses on the synthesis and applications of functional nanomaterials, and science education.



Shaowei Chen received his B.S. degree in chemistry from the University of Science and Technology of China in 1991, and M.S. and Ph.D. degrees from the Cornell University in 1993 and 1996, respectively. Following a postdoctoral appointment at the University of North Carolina Chapel Hill, he started his independent career in Southern Illinois University in 1998. In 2004, he moved to the University of California Santa Cruz and is currently a professor of chemistry. His research interests are primarily focused on functional nanocomposites, and their applications in electrochemical energy technologies and as antimicrobial agents.